المؤتمر الدولي الثالث للعلوم الهندسية

III. International Conference on Engineering Sciences

Rimar Academy
Publishing House

المؤتمر الدولي الثالث للعلوم الهندسية

III. International Conference on Engineering Sciences

FULL TEXT BOOK

2025

ISBN 978-625-92439-3-1

Publishing House:	دار النشر:	Rimar Academy
Editor:	المحرر:	Prof. Dr. Ghuson H. MOHAMMED
Publication Coordinator:	تنسيق النشر:	AMIR MUAENI
ISBN:	نظام الترميز الدولي لترقيم الكتاب:	**978-625-92439-3-1**
DOI :	رقم معرف الكائن الرقمي:	http://dx.doi.org/10.47832/EngConf3
Printing:	تاريخ الطباعة:	**27 / 02 / 2026**
Date of The Congress:	تاريخ المؤتمر:	**18 - 19 - 20 / 12 / 2025**
Pages:	عدد الصفحات:	**49**
URL:	رابط النشر:	www.rimaracademy.com
Certificate Printing Press Number	رقم شهادة المطبعة:	**47843**

PREFACE

III. International Conference on Engineering Sciences was organized by Mardin University in collaboration with Rimar Academy. The primary objective of this event was to compile and disseminate valuable scientific knowledge andmake ameaningful contribution to the future.

A substantial number of researchers from both local and international backgrounds demonstrated their interest in this conference. The scientific committee meticulously reviewed the submissions and ultimately accepted a select group of applicants—10 in total—of whom 6 were approved by the scientific committee.

The core of this conference was the presentation of 3 full research papers, while the remaining articles and research findings are set to be featured in for the coming issues of the MINAR Journal.

I would like to extend my sincere appreciation to all the contributors and scholars who played an essential role in making this conference a resounding success.
Your dedication and valuable contributions are deeply respected and acknowledged.

Editor-in-Chief
Prof. Dr. Ghuson H. MOHAMMED

رئيس المؤتمر
CHAIR OF CONGRESS

Prof. Dr. Ghuson H. MOHAMMED

Baghdad University

الرؤساء الفخريون
HONORARY COMMITTEE

Prof. Dr..Zakaria ZALLAM

Gaziantep University

Türkiye

Prof. Dr. Waad Mahmood RAOOF

Rector of Tikrit University

Iraq

Prof. Dr. Tariq Hafdhi Abbd Tawfeeq

President of Al-Farahidi University

Iraq

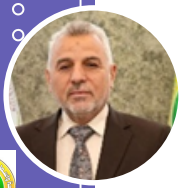

Prof Dr Abbas Lafta Kneehr

Rector of the University of Wasit

Iraq

Prof. Dr. Alyaa A. Ali Al-ATTAR

Rector of Northern Technical University

Iraq

Prof.Dr.Thaar S Al-Gasham

Rector of the University of Wasit

Iraq

الهيئة التحضيرية
ORGANIZING COMMITTEE

Prof. Dr. Abbas Fadhil Ibrahim

University of Technology

Iraq

Prof. Yasser Estanbouli

Aleppo University

syria

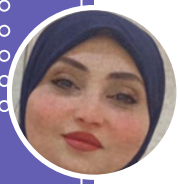

Dr. Muna Faeq Ali Al-Araji

University of Baghdad

Iraq

Dr. Lamya M. J. Mahdi Al-Saeed

University of Technology

Iraq

Dr.Ali Abed Asal Al-Graiti

college of engieering

Iraq

Dr. Hadeel Mowaffaq Mahmood Al Qaicy

University of Technology

Iraq

Dr.Rehab Mahmoud Ibrahim Ibrahim sayed ahmed

University of Engineering and Technology

Egypt

Dr. Marwan Kadhim Mohammed

University of Baghdad

Iraq

Lect. Dr.Ahmad N.AL-SHAMMAA

University of Baghdad

Iraq

Lec. Dr. Aws M. Abdullah

University of Baghdad

Iraq

الهيئة العلمية
SCIENTIFIC COMMITTEE

Prof. Dr. Abbas Fadhil Ibrahim

University of Technology

Iraq

Prof. Dr. Mahmoud Ahmed Hammoud Daoud

University of Mosul

Iraq

Dr. Aseel Younis Khalaf

Tikrit University

Iraq

Dr. Ahmed Khalid Ibrahim

UNIVERSITY OF MOSUL

Iraq

Assist. Prof. Dr. Mohammed Salih Ahmed

Tikrit University

Iraq

Dr.Buthaina S. Aziz

Southern Technical University

Iraq

Dr. Sawsan Dheyaa Mahmood

University Of Diyala

Iraq

Lec.Dr. Bilal Ahmed Hbeeb

University of technology

Iraq

INDEX

Qualitative Analysis of Generalized Caputo Volterra-Fredholm Integro-Differential Equations

Riyam Bassim Abdulmaged [1]

Ihab Hadi Jumaah [2]

Ali Farhan Hashoosh [3]

Alan Jalal Abdulqader [4]

Abstract:

The fractional generalized Caput Volterra-Fredholm integro-differential equation (GFCV-FIDE) with non-local condition is investigated in this work. It uses the Banach's fixed-point theorem (FPT) to demonstrate the existence and uniqueness of solutions. Additionally, it illustrates a noteworthy finding on the presence of a minimum of one solution, supported by criteria derived from the Krasnoselskii FPT. Ulam stability of the GFCV-FIDE is also investigated by using the Gronwall inequality. An example is shown to demonstrate the findings' robustness and practical usefulness.

2020 AMS Classification: 45J05; 47H10; 45M10.

Keywords and phrases: *Volterra-Fredholm Equation; Generalized Caputo Fractional; Derivative; Fixed-Point Theorem.*

http://dx.doi.org/10.47832/EngConf3-1

[1] Researcher. College of Education, Mustansiriyah University, Iraq
riyam.basim2023@uomustansiriyah.edu.iq

[2] Researcher. College of Education, Mustansiriyah University, Iraq ihabhadi5@uomustansiriyah.edu.iq

[3] Researcher. College of Basic Education, Misan University, Iraq ali_fr@uomisan.edu.iq

[4] Researcher. College of Education, Mustansiriyah University, Iraq alanjalal515@uomustansiriyah.edu.iq

1. Introduction

Fractional calculus extends the classical concepts of integration and differentiation of integer order to derivatives and integrals of arbitrary real (or even complex) order. Although fractional calculus has gained considerable attention in recent decades due to its wide range of applications, its origins date back to the correspondence between L'Hôpital and G.W. Leibniz in 1695. The theory was further developed by several mathematicians, including Euler, Laplace, Liouville, Riemann, Grünwald, Letnikov, Weyl, and Caputo (see [8,9] for historical details). Over time, these contributions established the theoretical foundation of modern fractional calculus.

One of the best mathematical instruments for characterizing the memory characteristics of certain materials and complicated systems is fractional calculus [22]. The integer-order derivative is commonly used in the classical framework to represent a system's memory:

$$\frac{dQ(z)}{dz} = \lim_{\Delta z \to 0} \frac{Q(z) - Q(z - \Delta z)}{\Delta z}, \qquad 0 < z$$

Because it only uses the function's values at two places, this definition accurately describes the system's short memory characteristics. On the other hand, the fractional approach uses the fractional order derivative to express a system's memory [19]:

$$\frac{d^{\theta} Q(z)}{dz^{\theta}} = \lim_{\mu \to 0} \mu^{-\theta} \sum_{r=0}^{n} (-1)^r \binom{\theta}{r} Q(z - r\mu), \qquad n\mu = z\ , \qquad 0 < \theta < 1$$

where the fractional derivative (FD) order is θ. The fractional derivative, in contrast to the classical derivative, takes into consideration the history of the function. In order to calculate the FD at a particular time t, the system's long memory qualities must be reflected by taking into account all of the function $\Phi(t)$'s prior values. For further information, see [23].

The large number of derivatives and integrals that are available in classical fractional calculus is one of its advantages. To improve our comprehension of the cosmos, fresh developments and advancements in this sector have always been required. Atangana and Baleanu presented a FD in the sense of Caputo in [7], which is notable as the ABC-fractional derivative, using the Mittag-Leffler function with non-singular kernels. Refer to [4, 12, 20, 25] for further information on FDs with non-singular kernels. In order to unify the Hadamard and Riemann-Liouville fractional operators, Katugampola presented what he dubbed generalized fractional operators [1, 2, 3, 18, 26]. Later, the Caputo and Caputo-Hadamard fractional derivatives were included in these generalized derivatives [11].

New fractional operators based on proportionate derivatives of one function with respect to another were presented by the authors in [14]. Depending on the particular function being utilized, the kernel in the suggested fractional operators contains an exponential function.

In many scientific domains, including physics, engineering, medicine, electrochemistry, control theory, and more, fractional differential equations (FDEs) naturally occur (see [10, 27, 28]). Many scholars have been inspired to examine both the quantitative and qualitative

elements of these equations due to their efficacy in simulating a wide range of real-world phenomena. Furthermore, FDEs with non-local conditions are a very interesting and pertinent field of study. The growing number of published works addressing the existence and uniqueness of solutions for this sort of equation is proof that scholars are becoming more and more interested in studying these equations. The vitality of research in this field is reflected in this trend. We can mention the following publications about the existence and uniqueness of solutions to fractional differential equations:

The existence and uniqueness of solutions to the following two Deformable FDEs were examined by the authors in [16]:

$$\begin{cases} {}^{\mathcal{D}\mathcal{D}}D^{\mathcal{T}}E(r) = \mathcal{F}(r, E(r)), \quad r \in [0, b] \\ E(0) + h(E) = E_0 \end{cases}$$

and

$$\begin{cases} {}^{\mathcal{D}\mathcal{D}}D^{T}E(r) = \mathcal{B}\big(E(r)\big) + \mathcal{F}\big(r, E[r]\big) + \int_0^r \mathcal{K}\big(r, s, E(r)\big)ds\,, r \in [0, b] \\ E(0) = E_0 \end{cases}$$

where the Deformable fractional derivative of order 0 < τ < 1 is represented by DDDτ ().

The following fractional perturbed neutral integro-differential issue involving the Deformable derivative

was examined by the authors of [24] to determine whether a solution exists and whether it is unique in a Banach space $\mathcal{X}$:

$$\begin{cases} {}^{\mathcal{D}\mathcal{D}}D^{T}E(r) - \mathcal{M}(r, E(\mu))) = \mathcal{L}(r, E(r), \int_0^r \mathcal{K}(r, \mathcal{Z}, E(r))dz) + \mathcal{F}\left(r, E(r), \int_0^r \mathcal{K}\big(r, z, E(r)\big)dz\right) \\ E(0) = E_0 \in X\,, r \in [0, b]\,, 0 < T < 1 \end{cases}$$

where . $\mathcal{M}: [0, B] \times X \to X$ in sominanuly diffronsiable lunction, $\mathcal{L}, \mathcal{F}: [\beta, b] \times X \times X \to X$ be continuous functions, and $\mathcal{K} \in (c(\mathcal{Z}\,, X\,)$ *where* $\mathcal{Z} := \{(r, z): 0 < z < r < b\}$.

Building on the aforementioned works, this paper examinsa the exiderse and uniquentes of the melution to the GIVI-FIDE with a now-local conditicion :

$$\begin{cases} {}_{\rho}^{C}D_{0^+}^{\tau,\mathcal{R}}\big({}_{\rho}^{C}D_{0^+}^{\delta,\mathcal{R}}\mathcal{H}(\mu) - \mathcal{B}(\mu, \mathcal{H}(\mu), \mathcal{G}\mathcal{H}(\mu)), \mathcal{U}\mathcal{H}(\mu)\big) = \mathcal{F}(\mu, \mathcal{H}(\mu), \mathcal{G}\mathcal{H}(\mu), \mathcal{U}\mathcal{H}(\mu)), \\ (\mathcal{H}(\mu) - \mathcal{B}(\mu, \mathcal{H}(\mu), \mathcal{G}\mathcal{H}(\mu), \mathcal{U}\mathcal{H}(\mu)))_{\mu=0} = u_0, \\ \big(\mathcal{H}(\mu) - \mathcal{B}(\mu, \mathcal{H}(\mu), \mathcal{G}\mathcal{H}(\mu), \mathcal{U}\mathcal{H}(\mu)\big)'_{\mu=0} = 0, \\ (\mathcal{H}(\mu) - \mathcal{B}(\mu, \mathcal{H}(\mu), \mathcal{G}\mathcal{H}(\mu), \mathcal{U}\mathcal{H}(\mu)))_{\mu=b} + \varphi(\mathcal{H}) = u_1, \mu \in \chi := [0, b], \end{cases}$$

where $1 < \tau < 2, 0 < \delta < 1$, ${}_{\rho}^{C}D_{0^+}^{\tau,\mathcal{R}}(\cdot)$ is the generalized Caputo proportional FD of order $\tau, \mathcal{R}: \chi \to \mathbb{R}, \mathcal{B}, \mathcal{F}: \chi \times \mathcal{X} \times \mathcal{X} \longrightarrow \mathcal{X}$ are continuous functions, $\varphi \in C(\mathcal{X}, \mathcal{X})$, and $u_0, u_1 \in \mathcal{X}$, where $\mathcal{X}$ is a Banach space. The operators $\mathcal{G}\mathcal{H}(\mu), \mathcal{U}\mathcal{H}(\mu)$ be given by

$$\mathcal{G}\mathcal{H}(\mu) := \int_0^{\mu} \Pi(\mu, s)\mathcal{H}(s)ds, \mathcal{U}\mathcal{H}(\mu) := \int_0^{b} \Pi_1(\mu, s)\mathcal{H}(s)ds$$

such that $\Pi_1\Pi_1 \in C(\mathfrak{D}, x)$, where $\mathfrak{D} := \{(\mu, \mathrm{s}): 0 < s < \mu < \mathrm{b}\}$. We consider

$$\mathcal{G}^* = \max_{\mu \in [0,b]} \int_0^{\mu} \|\Pi(\mu, s)\|ds, \mathcal{U}^* = \max_{\mu \in [0,b]} \int_0^{b} \|\Pi_1(\mu, s)\|ds$$

The following is a summary of this study's main contributions:

1. We use the FD instead of the classical derivative based on the previously described benefits and results of the fractional derivative.

2. To our know ledge, this is the first attempt to analyze the structure of the system introduced in (1) with a non-local condition.

3. We give the integral solution to the given system (1) (Lemma 2.5) using the features of the generalized Caputo FD type.

4. Banach and Krasnoselskii's alternative FPTs are used to establish the main existence theorems. Additionally, section 4 presents an instructive instances to show how the major results might be used.

5. Furthermore, this work builds upon and improves upon earlier research that has been published in the literature, such as that which is cited in [6,21].

2. Preliminaries

This section presents the solution formula for the nonlinear GFCV-FIDE (1) as well as definitions and lemmas pertaining to the generalized Caputo proportional FD. The subsequent sections of this work will make consistent use of these definitions and lemmas.

• Let $\chi = [0, b]$ be a finite interval of R . We denote by $C(\chi, \mathcal{X})$ the Banach space of all continuous functions with the norm $\|\mathcal{H}\| = \sup\{|\mathcal{H}(\mu)|: \mu \in \chi\}$.

• In this study, we consider the function $\mathcal{R}: \chi \to \mathbb{R}$ to be increasing, strictly positive, and differentiable.

Definition 2.1. [14]. Let $0 < \rho < 1, \tau > 0$, and f be a continuous function. The left-sided generalized proportional fractional integral of order τ with respect to $\mathcal{R}$ of the function f is determined by

$$ {}_{\rho}I_{0^+}^{\tau,\mathcal{R}} f(\mu) = \frac{1}{\rho^{\tau}\Gamma(\tau)} \int_0^{\mu} e^{\frac{\rho-1}{\rho}(\mathcal{R}(\mu)-\mathcal{R}(s))} \mathcal{R}'(s)(\mathcal{R}(\mu) - \mathcal{R}(s))^{\tau-1} f(s) ds $$

where $\Gamma(\tau) = \int_0^{+\infty} e^{-t} t^{\tau-1} dt$ is the Euler gamma function.

Dufinition 2.2. $||4$. Let $p \in [\Phi, \Psi], 4, W: |0,1| \times \mathbb{R} \to |0, \infty\rangle$ be cretinumse flunctions with $\lim_{p+0^+} \Phi(\beta, \mu) = 0$, $\lim_{p+1^-} \Phi(\beta, \mu) = 1$, $\lim_{p+0^+} \Psi(\beta, \mu) = 1$, $\lim_{p\to 1^-} \Psi(\beta, \mu) = 0$, and $\Phi(\beta, \mu) \neq 0, \rho \in (0,1), \Psi(\beta, \mu) \neq 0, p \in (0,1), a \in \mathbb{R}$. The properticrial detivalive of order ρ with respect to $\mathcal{R}$of the function f is cheleminal by

$$ {}_{\rho}D^{\mathcal{R}} f(\mu) = \Psi(\rho, \mu) f(\mu) + \Phi(\rho, \mu) \frac{f'(\mu)}{\mathcal{R}'(\mu)} $$

In particular, if $\Phi(\rho, \mu) = \rho$ and $\Psi(\rho, \mu) = 1 - \rho$, then we have

$$ {}_{\rho}D^{\mathcal{Q}} f(\mu) = (1 - \rho) f(\mu) + \rho \frac{f'(\mu)}{\mathcal{A}'(\mu)} $$

Definition 2.3. [14]. Let $\rho \in (0,1]$. The left-sided generalized Caputo proportional fractional derivative of order $n - 1 < \tau < n$ for the continuous function f is defined by

$$
\begin{aligned}
{}_{\rho}^{C}D_{0^+}^{\tau,\mathcal{P}} f(\mu) &= \rho I_{0^+}^{n-\tau,\mathcal{Q}}\left({}_{\rho}D^{n,\mathcal{P}} f(\mu)\right) \\
&= \frac{1}{\rho^{n-\tau}\Gamma(n-\tau)} \int_0^{\mu} e^{\frac{\rho-1}{\rho}(\mathcal{P}(\mu)-\mathcal{R}(s))} \mathcal{R}'(s)(\mathcal{R}(\mu)-\mathcal{R}(s))^{n-\tau-1}\left({}_{\rho}D^{n,\mathcal{R}} f\right)(s)ds
\end{aligned}
$$

where $n = [\tau] + 1$ and ${}_{\rho}D^{n\mathcal{Q}} = \underbrace{\rho D^{\mathcal{Q}}\ {}_{\rho}D_{\rho}^{\mathcal{P}} \ldots D^{\mathcal{Q}}}_{n-\text{ times}}$;

As a simplification, throughout this manuscript, we pose

$$\Omega_{\underline{Z}}^{\tau-1}(\mu,0) = e^{\frac{\rho-1}{\rho}(\mathcal{R}(\mu)-g(0))}(\mathcal{R}(\mu)-g(0))^{\tau-1}.$$

Lemma 2.1. [13]. Let $\mu \in \chi, \rho \in (0,1], \tau, \delta > 0$, and f be a continuous function. Then, we have

$$\rho I_{0+}^{\tau,\mathcal{B}}\left({}_{\rho}I_{0+}^{\delta,\mathcal{R}} f(\mu)\right) = \rho I_{0+}^{\tau,\mathcal{R}}\left({}_{\rho}I_{0+}^{\delta,\mathcal{P}} f(\mu)\right) = \rho I_{0+}^{\tau+\delta,\mathcal{P}} f(\mu)$$

Lemma 2.2. [13]. Let $\rho \in (0,1]$ and $\tau, \delta > 0$. Then, we have

(i) $\left({}_{\rho}I_{0+}^{T,\mathcal{R}} e^{\frac{\rho-1}{\rho}(\mathcal{B}(t)-\mathcal{Q}(0))}(\mathcal{R}(t)-\mathcal{R}(0))^{\delta-1}\right)(\mu) = \frac{\Gamma(\delta)}{\rho^{\Gamma}\Gamma(\tau+\delta)}\Omega_{\mathcal{R}}^{\tau+\delta-1}(\mu,0).$

(ii) ${}_{\rho}^{C}D_{0^+}^{\tau,\mathcal{R}} e^{\frac{\rho-1}{\rho}(\mathcal{R}(t)-\mathcal{Q}(0))}(\mathcal{R}(t)-\mathcal{R}(0))^{\delta-1}\Big)(\mu) = \frac{\rho^{\sigma}\Gamma(\delta)}{\Gamma(\delta-\tau)}\Omega_{\mathcal{R}}^{\delta-\tau-1}(\mu,0).$

Lemma 2.3. [13]. Let $\rho \in (0,1], \tau > 0$, and f be a continuous function. Then, we have

$$\lim_{\mu\to 0}\left(\rho I_{0+}^{\tau,\mathcal{P}} f(\mu)\right) = 0$$

Lemma 2.4. [15]. Let $\rho \in (0,1], n-1 < \tau < n, (n = [\tau]+1)$. Then, we have

$$\rho I_{0+}^{\tau,\mathcal{Q}}\left({}_{\rho}^{C}D_{0+}^{\tau,\mathcal{Q}} f(\mu)\right) = f(\mu) - \sum_{k=0}^{n-1} \frac{\left({}_{\rho}D^{k,\mathcal{P}} f\right)(0)}{\rho^{k}\Gamma(k+1)}\Omega_{\mathcal{B}}^{k}(\mu,0).$$

To simplify problem (1), we take the following problem and determine its solution formula:

$$
\begin{cases}
{}_{\rho}^{C}D_{0^+}^{\tau,\mathcal{R}}\left({}_{\rho}^{C}D_{0+}^{\delta,\mathcal{R}}(\mathcal{H}(\mu)-h(\mu))\right) = f(\mu), t \in \chi = [0,b] \\
(\mathcal{H}(\mu)-h(\mu))_{\mu=0} = u_0, (\mathcal{H}(\mu)-h(\mu))'_{\mu=0} = 0 \\
(\mathcal{H}(\mu)-h(\mu))_{\mu=b} + \varphi(\mathcal{H}) = u_1
\end{cases}
$$

where $0 < \tau < 1, 1 < \delta < 2$, ${}_{\rho}^{C}D_{0^+}^{\tau,\&}(\cdot)$ is the generalized Caputo proportional fractional derivative of order $\tau, h, f: \chi \longrightarrow \mathcal{X}$ be continuous functions, and $\varphi \in C(\mathcal{X},\mathcal{X})$.

Lemma 2.5. Let $h, f: \chi \longrightarrow \mathcal{X}$ be continuous functions. Hence, the system (3) has a solution provided by

$$
\begin{aligned}
\mathcal{H}(\mu) = &\frac{(\Delta-\varphi(\mathcal{H}))}{\Omega_{\mathcal{R}}^{\delta}(b,0)}\Omega_{\mathcal{R}}^{\delta}(\mu,0) + u_0 e^{\frac{\rho-1}{\rho}(\mathcal{R}(\mu)-\mathcal{R}(0))} + \frac{(1-\rho)u_0}{\rho}\Omega_{\mathcal{R}}^{1}(\mu,0) \\
&+ \frac{1}{\rho^{\delta+\tau}\Gamma(\delta+\tau)}\int_0^{\mu} \Omega_{\mathcal{R}}^{\delta+\tau-1}(\mu,s)\mathcal{R}'(s)f(s)ds + h(\mu), \mu \in [0,b]
\end{aligned}
$$

where $\Omega_{\mathcal{R}}^{(\cdot)}(\mu,.) and \Delta$ are given by (2) and (4), respectively.

Proof. Let $\mathcal{H}(\mu)$ be a solution of the problem (1). Applying the operator $\rho_{0^+}^{\tau,\mathcal{R}}(\cdot)$ to both sides of (3) and from Lemma 2.4, we get

$$ {}_{\rho}^{C}D_{0^+}^{\delta,\mathcal{R}}(\mathcal{H}(\mu)-h(\mu)) = \beta_1 e^{\frac{\rho-1}{\rho}(\mathcal{R}(\mu)-\mathcal{R}(0))} + {}_{\rho}I_{0^+}^{\tau,\mathcal{R}} f(\mu) $$

with $\beta_1 \in \mathbb{R}$. Next, Applying the operator ${}_{\rho}I_{0^+}^{\delta,\mathcal{R}}(\cdot)$ to both sides of (5), we get

$$ \mathcal{H}(\mu)-h(\mu) = \beta_1 {}_{\rho}I_{0^+}^{\delta,\mathcal{R}}\Omega_{\mathcal{R}}^{0}(\mu,0) + \beta_2\Omega_{\mathcal{R}}^{0}(\mu,0) + \beta_3\frac{\Omega_{\mathcal{R}}^{1}(\mu,0)}{\rho} + \rho I_{0^+}^{\tau+\delta,\mathcal{R}} f(\mu), $$

with $\beta_1,\beta_2,\beta_3 \in \mathbb{R}$. Using Lemma 2.2$(i)$, then the integral equation (6) becomes

$$ \begin{aligned} \mathcal{H}(\mu)-h(\mu) = {} & \beta_1\frac{e^{\frac{\rho-1}{\rho}(\mathcal{R}(\mu)-\mathcal{R}(0))}(\mathcal{R}(\mu)-\mathcal{R}(0))^{\delta}}{\rho^{\delta}\Gamma(\delta+1)} + \beta_2 e^{\frac{\rho-1}{\rho}(\mathcal{R}(\mu)-\mathcal{R}(0))} \\ & + \beta_3\frac{e^{\frac{\rho-1}{\rho}(\mathcal{R}(\mu)-\mathcal{R}(0))}(\mathcal{R}(\mu)-\mathcal{R}(0))}{\rho} \\ & + \frac{1}{\rho^{\delta+\tau}\Gamma(\delta+\tau)}\int_0^{\mu} e^{\frac{\rho-1}{\rho}(\mathcal{R}(\mu)-\mathcal{R}(s))}(\mathcal{R}(\mu)-\mathcal{R}(s))^{\delta+\tau-1}\mathcal{R}'(s)f(s)ds \end{aligned} $$

Putting $\mu = 0$ in the integral equation (7), we get $\beta_2 = (\mathcal{H}(\mu)-h(\mu))_{\mu=0} = u_0$. From the integral equation (7), with $\beta_2 = u_0$, we get

$$ \begin{aligned} (\mathcal{H}(\mu)-h(\mu))' = {} & \frac{\beta_1}{\rho^{\delta}\Gamma(\delta+1)}\left(\frac{\mathcal{R}'(\mu)(\rho-1)}{\rho}\Omega_{\mathcal{R}}^{\delta}(\mu,0) + \delta'(\mu)\Omega_{\mathcal{R}}^{\delta-1}(\mu,0)\right) \\ & + \frac{u_0\mathcal{R}'(\mu)(\rho-1)}{\rho}e^{\frac{\rho-1}{\rho}(\mathcal{R}(\mu)-\mathcal{R}(0))} \\ & + \frac{\beta_3}{\rho}\left(\mathcal{R}'(\mu)e^{\frac{\rho-1}{\rho}(\mathcal{R}(\mu)-\mathcal{R}(0))} + \frac{\mathcal{R}'(\mu)(\rho-1)\Omega_{\mathcal{R}}^{1}(\rho,0)}{\rho}\right) \\ & + \frac{\mathcal{R}'(\mu)(\rho-1)}{\rho^{\delta+\tau+1}\Gamma(\delta+\tau)}\int_0^{\mu}\Omega_{\mathcal{R}}^{\delta+\tau-1}(\mu,s)\mathcal{R}'(s)f(s)ds \\ & + \frac{\mathcal{R}'(\mu)}{\rho^{\delta+\tau}\Gamma(\delta+\tau-1)}\int_0^{\mu}\Omega_{\mathcal{R}}^{\delta+\tau-2}(\mu,s)\mathcal{R}'(s)f(s)ds \end{aligned} $$

Taking $\mu = 0$ in the integral equation (8), we obtain $\beta_3 = u_0(1-\rho)$. Now, taking $\mu = b, \beta_2 = u_0$, and $\beta_3 = u_0(1-\rho)$ in the integral equation (7), we obtain

$$ \begin{aligned} (\mathcal{H}(\mu)-h(\mu))_{\mu=b} = {} & \beta_1\frac{\Omega_{\mathcal{R}}^{\delta}(b,0)}{\rho^{\delta}\Gamma(\delta+1)} + u_0 e^{\frac{\rho-1}{\rho}(\mathcal{B}(b)-\mathcal{R}(0))} \\ & + u_0(1-\rho)\frac{\Omega_{\mathcal{R}}^{1}(b,0)}{\Omega} + \rho I_{0+}^{\delta+\tau,\mathcal{R}} f(b) \end{aligned} $$

Using the condition $(\mathcal{H}\ (\mu) - h(\mu)\mu{=}b + \varphi(\mathcal{H}) = u_1$, we obtain

$$ \begin{aligned} \beta_1 &= \frac{\rho^{\delta}\Gamma(\delta+1)}{\Omega_{\mathcal{Z}}^{\delta}(b,0)}\left(u_1 - \varphi(\mathcal{H}) - u_0 e^{\frac{\rho-1}{\rho}(\mathcal{P}(b)-\mathcal{H}(0))} - u_0(1-\rho)\frac{\Omega_{\mathcal{Z}}^{1}(b,0)}{\rho} - \rho I_{0^+}^{\delta+\tau,\mathcal{R}} f(b)\right) \\ &= \frac{\rho^{\delta}\Gamma(\delta+1)}{\Omega_{\mathcal{R}}^{\delta}(b,0)}(\Delta - \varphi(\mathcal{H})) \end{aligned} $$

where

$$ \Delta = u_1 - u_0\left(e^{\frac{\rho-1}{\rho}(\mathcal{R}(b)-\mathcal{Q}(0))} + (1-\rho)\frac{\Omega_{\mathcal{Z}}^{1}(b,0)}{\rho}\right) - \rho I_{0^+}^{\delta+\tau,\mathcal{Q}} f(b) $$

Substituting β_1,β_2, and β_3 in (7) we have

$$\mathcal{H}(\mu) = \frac{(\Delta - \varphi(\mathcal{H}))}{\Omega_{\mathcal{Z}}^{\delta}(b,0)}\Omega_{\mathcal{Z}}^{\delta}(\mu,0) + u_0 e^{\frac{\rho-1}{\rho}(\mathcal{P}(\mu)-\mathcal{P}(0))} + \frac{(1-\rho)u_0}{\rho}\Omega_{\mathcal{Z}}^{1}(\mu,0)$$
$$+ \frac{1}{\rho^{\delta+\tau}\Gamma(\delta+\tau)}\int_0^{\mu} \Omega_{\mathcal{G}}^{\delta+\tau-1}(\mu,s)\mathcal{R}'(s)f(s)ds + h(\mu)$$

The evidence is now complete.

We can now define the solution to the GCFV-FIDE (1) using the data from the preceding lemma.

Definition 2.4. If $\mathcal{H}$ solves the problem (1), then $\mathcal{H}$ also solves the integral equation that follows:

$$\mathcal{H}(\mu) = \frac{(\Delta - \varphi(\mathcal{H}))}{\Omega_{\mathcal{B}}^{\delta}(b,0)}\Omega_{\mathcal{B}}^{\delta}(\mu,0) + u_0 e^{\frac{\rho-1}{\rho}(\mathcal{R}(\mu)-\mathcal{E}(0))} + \frac{(1-\rho)u_0}{\rho}\Omega_{\mathcal{G}}^{1}(\mu,0) + \frac{1}{\rho^{\delta+\tau}\Gamma(\delta+\tau)}$$
$$\times \int_0^{\mu} \Omega_{\mathcal{G}}^{\delta+\tau-1}(\mu,s)\mathcal{R}'(s)\mathcal{F}(s,\mathcal{H}(s),\mathcal{G}\mathcal{H}(s),\mathcal{U}\mathcal{H}(s))ds + \mathcal{H}(\mu,\mathcal{H}(\mu),\mathcal{G}\mathcal{H}(\mu),\mathcal{U}\mathcal{H}(\mu)),$$

as long as the integral mentioned above is finite.

3. Existence and uniqueness results

In this section, we present and study the existence of solutions for the given nonlinear GCFV-FIDE (1) under the Krasnoselskiis FPT.

Theorem 3.1. [5] Let $\mathcal{X}$ be a convex, closed, and nonempty subset of the Banach algebra $\mathcal{X}$. We consider the two operators $\mathcal{N}, \mathcal{S}: \mathcal{X} \to \mathcal{X}$ such that:

(a) $\mathcal{N}u + \mathcal{S}v \in \mathcal{X}, \forall u, v \in \mathcal{X}$.

(b) $\mathcal{N}$ is a contraction on $\mathcal{X}$.

(c) $\mathcal{Y}$is completely continuous on $\mathcal{X}$.

Then, the operator $\mathcal{P}u = \mathcal{N}u + \mathcal{Y}u$ has at least a fixed point in $\mathcal{X}$.

The following presumptions are necessary in order to apply the Krasnoselskiis FPT:

(A_1) The function $\mathcal{F}: \chi \times \mathcal{X}^3 \longrightarrow \mathcal{X}$ is continuous and there are constants $L_y, \hat{L}_y$, and $\bar{L}_y$ such that for all $v, w, z, v', w', z' \in \mathcal{X}$ and for all $\mu \in \chi$, we have

(i) $\|\mathcal{F}(\mu, v, w, z) - \mathcal{F}(\mu, v', w', z')\| \leq L_{\mathcal{S}}[\|v - v'\| + \|w - w'\| + \|z - z'\|]$.

(ii) $\|\mathcal{F}(\mu, v, w, z)\| \leq \hat{L}_{\mathcal{S}} + \bar{L}_{\mathcal{S}}[\|v\| + \|w\| + \|z\|]$.

(A_2) The function $\mathcal{B}: \chi \times \mathcal{X}^3 \longrightarrow \mathcal{X}$ is continuous and there are constants $M_{\mathcal{A}}, \widehat{M}_{\mathcal{B}}$, and $\bar{M}_{\mathcal{B}}$ such that for all $v, w, v', w', z' \in \mathcal{X}$ and for all $\mu \in \chi$, we have

(i) $\|\mathcal{B}(\mu, v, w, z) - \mathcal{B}(\mu, v', w', z')\| \leq M_{\mathcal{S}\mathcal{B}}[\|v - v'\| + \|w - w'\| + \|z - z'\|]$.

(ii) $\|\mathcal{B}(\mu, v, w, z)\| \leq \widehat{M}_{\mathcal{B}} + \bar{M}_{\mathcal{B}}[\|v\| + \|w\| + \|z\|]$.

(A_3) The function $\bar{\varphi}: \mathcal{X} \longrightarrow \mathcal{X}$ is continuous and there are constants $K_{\varphi}, \hat{K}_{\varphi}$, and $\bar{K}_{\varphi}$ such that for all $v, w, z \in \mathcal{X}$ and for all $\mu \in \chi$, we have

(i) $\|\varphi(v) - \varphi(w)\| \leq K_{\varphi}\|v - w\|$.

(ii) $\|\varphi(v)\| \leq \hat{K}_{\varphi} + \bar{K}_{\varphi}\|v\|$.

Let the Banach space $\mathcal{Q} := (\mathcal{C}(\chi, \mathcal{X}), \|\cdot\|)$. Then we consider the subset $\mathcal{S}$ of $\mathcal{Q}$ given by:

$$\mathcal{S} = \{\mathcal{H} \in \mathcal{Q}: \|\mathcal{H}\| \leq \Theta\}$$

with

$$\Theta > \frac{\widehat{\Psi}}{1-\Phi}, \text{ such that } 1-\bar{\Psi} \neq 0$$

where

$$\widehat{\Psi}' = \frac{(\mathcal{R}(b)-\mathcal{R}(0))^{\delta}}{\Omega_{\mathcal{B}}^{\delta}(b,0)}\left(\|\Delta\| + \hat{K}_{\varphi}\right) + \|u_0\|\left|1-\frac{1-\rho}{\rho}(\mathcal{R}(b)-\mathcal{R}(0))\right| + \frac{(\mathcal{R}(b)-\mathcal{R}(0))^{\delta+\tau}\hat{L}_{\mathcal{S}}}{\rho^{\delta+\tau}\Gamma(\delta+\tau+1)} + \widehat{M}_{\mathcal{B}}$$

$$\bar{\Psi}' = \frac{(\mathcal{R}(b)-\mathcal{R}(0))^{\delta}\bar{K}_{\varphi}}{\Omega_{\mathcal{B}}^{\delta}(b,0)} + \frac{(\mathcal{R}(b)-\mathcal{R}(0))^{\delta+\tau}\bar{L}_{\mathcal{S}}(1+\mathcal{G}^*+\mathcal{Z}^*)}{\rho^{\delta+\tau}\Gamma(\delta+\tau+1)} + \bar{M}_{\mathcal{C}}(1+\mathcal{G}^*+\mathcal{C}^*)$$

An obvious subset of the Banach space $\mathcal{Q}$ is $\mathcal{S}$, which is convex, bounded, closed, and nonempty. We now possess all the arguments required to prove the existence results for the specified system (1). As a result, the following existence theorem is presented.

Theorem 3.2. Suppose that all assumptions $(A_1)-(A_3)$ hold and

$$\frac{(\mathcal{R}(b)-\mathcal{R}(0)))^{\delta}}{\Omega_{\mathcal{B}}^{\delta}(b,0)}K_{\varphi} < 1$$

where $\Omega_{\mathcal{B}}^{(\cdot)}(.,0)$ is given by (2). Then, the system (1) has at least a solution $\mathcal{H} \in \mathcal{C}(\chi,\mathcal{X})$. Proof. To apply the Krasnoselskiis FPT, we define the operators $\mathcal{Y}:\mathcal{S}\longrightarrow\mathcal{X}, \mathcal{W}:\mathcal{S}\longrightarrow\mathcal{X}$, and $\mathcal{P}:\mathcal{S}\longrightarrow\mathcal{X}$ as follows:

$$(\mathcal{V}\mathcal{H})(\mu) = \frac{(\Delta-\varphi(\mathcal{H}))}{\Omega_{\mathcal{B}}^{\delta}(b,0)}\Omega_{\mathcal{R}}^{\delta}(\mu,0) + u_0 e^{\frac{\rho-1}{\rho}(\mathcal{B}(\mu)-\mathcal{B}(0))} + \frac{(1-\rho)u_0}{\rho}\Omega_{\mathcal{H}}^{1}(\mu,0)$$

$$(\mathcal{H}\mathcal{H})(\mu) = \frac{1}{\rho^{\delta+\tau}\Gamma(\delta+\tau)} \times \int_0^{\mu}\Omega_{\mathcal{R}}^{\delta+\tau-1}(\mu,s)\mathcal{R}'(s)\mathcal{F}(s,\mathcal{H}(s),\mathcal{G}\mathcal{H}(s),\mathcal{Z}\mathcal{H}(s))ds + \mathcal{B}(\mu,\mathcal{H}(\mu),\mathcal{G}\mathcal{H}(\mu),\mathcal{Z}\mathcal{H}(\mu))$$

$$(\mathcal{P}\mathcal{H})(\mu) = ((\mathcal{V}+\mathcal{H})\mathcal{H})(\mu)$$

The proof is then provided in the subsequent steps: Step 1: Let $\mu \in [0,b]$ and $\mathcal{H},v \in \mathcal{S}$. By using the assumptions $(A_1)(ii),(A_2)(ii),(A_3)(ii)$, and the fact that

$$e^{\frac{p-1}{p}(\mathcal{B}(\mu)-\mathcal{B}(0))} < 1,$$

we get

$$
\begin{aligned}
&\|\mathcal{V}(\mu)+\mathcal{W}v(\mu)\|\\
&=\|\frac{(\Delta-\varphi(\mathcal{H}))}{\Omega_{\mathcal{B}}^{\delta}(b,0)}\Omega_{\underline{\mathcal{Z}}}^{\delta}(\mu,0)+u_0e^{\frac{\rho-1}{\rho}(\mathcal{B}(\mu)-\mathcal{B}(0))}+\frac{(1-\rho)u_0}{\rho}\Omega_{\underline{\mathcal{Z}}}^{1}(\mu,0)\\
&+\frac{1}{\rho^{\delta+\tau}\Gamma(\delta+\tau)}\int_0^{\mu}\Omega_{\mathcal{A}}^{\delta+\tau-1}(\mu,s)\mathcal{R}'(s)\mathcal{F}(s,v(s),\mathcal{G}v(s),\mathcal{Z}v(s))ds+\mathcal{B}(\mu,v(\mu),\mathcal{G}v(\mu),\mathcal{Z}v(\mu))\|\\
&\leq\frac{(\mathcal{R}(b)-\mathcal{R}(0))^{\delta}}{\Omega_{\mathcal{B}}^{\delta}(b,0)}\left(\|\Delta\|+\hat{K}_{\varphi}+\bar{K}_{\varphi}\|\mathcal{H}\|\right)+\|u_0\|\left|1-\frac{1-\rho}{\rho}(\mathcal{R}(b)-\mathcal{B}(0))\right|\\
&+\frac{1}{\rho^{\delta+\tau}\Gamma(\delta+\tau)}\int_0^{\mu}(\mathcal{R}(\mu)-\mathcal{R}(s))^{\delta+\tau-1}\mathcal{R}'(s)\left(\hat{L}_{\mathcal{S}}+\bar{L}_{\mathcal{S}}[\|v\|+\|\mathcal{G}v\|+\|\mathcal{Z}v\|]\right)ds\\
&+\hat{M}_{\mathcal{SB}}+\bar{M}_{\mathcal{SB}}[\|v\|+\|\mathcal{G}v\|+\|\mathcal{Z}v\|]\\
&\leq\frac{(\mathcal{R}(b)-\mathcal{R}(0))^{\delta}}{\Omega_{\mathcal{B}}^{\delta}(b,0)}\left(\|\Delta\|+\hat{K}_{\varphi}+\bar{K}_{\varphi}\Theta\right)+\|u_0\|\left|1-\frac{1-\rho}{\rho}(\mathcal{R}(b)-\mathcal{R}(0))\right|\\
&+\frac{(\mathcal{R}(b)-\mathcal{R}(0))^{\delta+\tau}}{\rho^{\delta+\tau}\Gamma(\delta+\tau+1)}\left(\hat{L}_{\mathcal{S}}+\bar{L}_{\mathcal{S}}\Theta(1+\mathcal{G}^*+\mathcal{U}^*)\right)+\hat{M}_{\mathcal{B}}+\bar{M}_{\mathcal{S}}\Theta(1+\mathcal{G}^*+\mathcal{U}^*)\Bigg)\\
&\leq\frac{(\mathcal{R}(b)-\mathcal{R}(0))^{\delta}}{\Omega_{\mathcal{B}}^{\delta}(b,0)}\left(\|\Delta\|+\hat{K}_{\varphi}\right)+\|u_0\|\left|1-\frac{1-\rho}{\rho}(\mathcal{B}(b)-\mathcal{B}(0))\right|\\
&+\frac{(\mathcal{R}(b)-\mathcal{R}(0))^{\delta+\tau}\hat{L}_{\mathcal{S}}}{\rho^{\delta+\tau}\Gamma\left(\delta+\tau+\hat{M}_{\mathcal{S}}\right.}\\
&+\Theta\left[\frac{(\mathcal{R}(b)-\mathcal{R}(0))^{\delta}\bar{K}_{\varphi}}{\Omega_{\mathcal{B}}^{\delta}(b,0)}+\frac{(\mathcal{R}(b)-\mathcal{R}(0))^{\delta+\tau}\bar{L}_{\mathcal{Y}}(1+\mathcal{G}^*+\mathcal{U}^*)}{\rho^{\delta+\tau}\Gamma(\delta+\tau+1)}+\bar{M}_{\mathcal{B}}(1+\mathcal{G}^*+\mathcal{U}^*)\right]\\
&\leq\hat{\Psi}+\Theta\bar{\Psi}<\Theta.
\end{aligned}
$$

Therefore, $\mathcal{V}(\mathcal{H})+\mathcal{W}(v)\in\mathcal{S}$ for all $\mathcal{H},v\in\mathcal{S}$.

Step 2: We show that $\mathcal{V}$ is a contraction. Let $\mu\in[0,b]$ and $\mathcal{H},v\in\mathcal{S}$. By using the assumption

$$(A_3)(i),$$

and the fact that

$$e^{\frac{p-1}{p}(\mathcal{R}(\mu)-\mathcal{R}(0))}<1,$$

we get

$$\|\mathcal{V}\mathcal{H}(\mu)-\mathcal{V}v(\mu)\|=\frac{\Omega_{\mathcal{B}}^{\delta}(\mu,0)}{\Omega_{\mathcal{G}}^{\delta}(b,0)}\|\varphi(\mathcal{H})-\varphi(v)\|\leq\frac{(\mathcal{R}(b)-\mathcal{R}(0)))^{\delta}}{\Omega_{\mathcal{R}}^{\delta}(b,0)}K_{\varphi}\|\mathcal{H}-v\|.$$

From the condition (11), we can deduce that the operator $\mathcal{Y}$ is a contraction.
Step 3: We show that the operator $\mathcal{W}$ is completely continuous.

(i) $\mathcal{W}$ is continuous:

Let $\mu\in[0,b]$ and $\mathcal{H}_n$ be a sequence of $\mathcal{S}$ such that $\mathcal{H}_n\longrightarrow\mathcal{H}^{\circ}$ as $n\longrightarrow\infty$ in $\mathcal{S}$. Then, we get

$$
\begin{aligned}
&\|\mathcal{W}\mathcal{H}_n(\mu)-\mathcal{W}\mathcal{H}(\mu)\|\\
&\leq\frac{1}{\rho^{\delta+\tau}\Gamma(\delta+\tau)}\\
&\times\int_0^{\mu}\Omega_{\mathcal{Q}}^{\delta+\tau-1}(\mu,s)\mathcal{E}'(s)\|\mathcal{F}(s,\mathcal{H}_n(s),\mathcal{G}\mathcal{H}_n(s),\mathcal{U}\mathcal{H}_n(s))-\mathcal{F}(s,\mathcal{H}(s),\mathcal{G}\mathcal{H}(s),\mathcal{U}\mathcal{H}(s))\|ds\\
&+\|\mathcal{B}(\mu,\mathcal{H}_n(\mu),\mathcal{G}\mathcal{H}_n(\mu),\mathcal{U}\mathcal{H}_n(\mu))-\mathcal{B}(\mu,\mathcal{H}(\mu),\mathcal{G}\mathcal{H}(\mu),\mathcal{U}\mathcal{H}(\mu))\|
\end{aligned}
$$

The Lebesgue dominated convergence theorem and the continuity of the functions $\mathcal{F}$ and $\mathcal{B}$ allow us to obtain.

$$\|\mathcal{W}\mathcal{H}_n(\mu) - \mathcal{W}\mathcal{H}(\mu)\| \longrightarrow 0, \text{ as } n \longrightarrow \infty.$$

This implies that the operator $\mathcal{W}$ is continuous.

(ii) $\mathcal{W}$ is uniformly bounded:

Let $\mu \in [0,b]$ and $\mathcal{H} \in \mathcal{S}$. Then, by using the assumptions $(A_1)(ii), (A_2)(ii)$, and the fact that

$$e^{\frac{P-1}{P}(\mathcal{R}(\mu)-\mathcal{P}(0))} < 1,$$

we get

$$\begin{aligned}
&\|\mathcal{W}\mathcal{H}(\mu)\| \\
&\leq \frac{1}{\rho^{\delta+\tau}\Gamma(\delta+\tau)} \\
&\times \int_0^{\mu} \Omega_{\mathcal{R}}^{\delta+\tau-1}(\mu,s)\mathcal{W}'(s)\|\mathcal{F}(s,\mathcal{H}(s),\mathcal{G}\mathcal{H}(s),\mathcal{Z}\mathcal{H}(s))\|ds + \|\mathcal{B}(\mu,\mathcal{H}(\mu),\mathcal{G}\mathcal{H}(\mu),\mathcal{Z}\mathcal{H}(\mu))\| \\
&\leq \frac{1}{\rho^{\delta+\tau}\Gamma(\delta+\tau)}\int_0^{\mu} (\mathcal{B}(\mu)-\mathcal{B}(s))^{\delta+\tau-1}\mathcal{B}'(s)\big(\hat{L}_y + \bar{L}_y[\|\mathcal{H}\| + \|\mathcal{G}\mathcal{H} + \|\mathcal{U}\mathcal{H}\|]\big)ds \\
&+\hat{M}_{\mathcal{C}} + \bar{M}_{\mathcal{C}}[\|\mathcal{H}\| + \|\mathcal{H}\| + \|\mathcal{Z}\mathcal{H}\|] \\
&\leq \frac{(\mathcal{R}(b)-\mathcal{R}(0))^{\delta+\tau}}{\rho^{\delta+\tau}\Gamma(\delta+\tau+1)}\Big(\hat{L}_y + \bar{L}_y\Theta(1+\mathcal{G}^*+\mathcal{Z}^*)\Big) + \hat{M}_{\mathcal{B}} + \bar{M}_{\mathcal{B}}\Theta(1+\mathcal{G}^*+\mathcal{Z}^*)
\end{aligned}$$

Then, the operator $\mathcal{W}$ is uniformly bounded.

(iii) $\mathcal{W}$ is equicontinuous:

Let $\mu_1, \mu_2 \in [0,b], (\mu_1 < \mu_2)$, and $\mathcal{H} \in \mathcal{S}$, by using our assumptions, we get

$$\begin{aligned}
&\|(\mathcal{W}\mathcal{H})(\mu_2) - (\mathcal{W}\mathcal{H})(\mu_1)\| \\
&= \|\frac{1}{p^{\delta+\tau}\Gamma(\delta+\tau)} \\
&\times \int_0^{\mu_2} \Omega_{\mathcal{B}}^{\delta+1}(\mu_2,s)\mathcal{R}'(s)\mathcal{F}(s,\mathcal{H}(s),\mathcal{G}\mathcal{H}(s),\mathcal{U}\mathcal{H}(s))ds + \mathcal{B}\big(\mu_2,\mathcal{H}(\mu_2),\mathcal{G}\mathcal{H}(\mu_2),\mathcal{U}\mathcal{H}(\mu_2)\big) \\
&-\frac{1}{\rho^{\delta+\tau}(\delta+\tau)} \\
&\times \int_0^{\mu_1} \Omega_{\mathcal{B}}^{\delta+\tau-1}(\mu_1,s)\mathcal{H}'(s)\mathcal{F}(s,\mathcal{H}(s),\mathcal{G}\mathcal{H}(s),\mathcal{U}\mathcal{H}(s))ds - \mathcal{B}\big(\mu_1,\mathcal{H}(\mu_1),\mathcal{G}\mathcal{H}(\mu_1),\mathcal{Z}\mathcal{H}(\mu_1)\big)\| \\
&= \|\frac{1}{\rho^{\delta+\tau}\Gamma(\delta+\tau)} \\
&\times \int_{\mu_1}^{\mu_2} \Omega_{\mathcal{B}}^{\delta+\tau-1}(\mu_2,s)^{\mathcal{B}}(s)\mathcal{F}(s,\mathcal{H}(s),\mathcal{G}\mathcal{H}(s),\mathcal{U}\mathcal{H}(s))ds + \mathcal{B}\big(\mu_2,\mathcal{H}(\mu_2),\mathcal{G}\mathcal{H}(\mu_2),\mathcal{U}\mathcal{H}(\mu_2)\big) \\
&+\frac{1}{\rho^{\delta+\tau}\Gamma(\delta+\tau)}\int_0^{\mu_1} \Big(\Omega_{\mathcal{G}}^{\delta+\tau-1}(\mu_2,s) - \Omega_{\mathcal{B}}^{\delta+\tau-1}(\mu_1,s)\Big)\mathcal{H}'(s)\mathcal{F}(s,\mathcal{H}(s),\mathcal{G}\mathcal{H}(s),\mathcal{Z}\mathcal{H}(s))ds \\
&-\mathcal{B}^{\left(\mu_1,\mathcal{H}'(\mu_1),\mathcal{Z}\mathcal{H}'(\mu_1),\mathbb{Z}\cdot\mathcal{H}'(\mu_1)\right)|} \\
&\leq \frac{\Big(\hat{L}_{\mathcal{S}} + \bar{L}_{\mathcal{S}}\Theta(1+\mathcal{G}^*+\mathcal{U}^*)\Big)}{\rho^{\delta+\tau}\Gamma(\delta+\tau)}\|\int_{\mu_1}^{\mu_2} (\mathcal{R}(\mu_2)-\mathcal{R}(s))^{\delta+\tau-1}\mathcal{R}'(s)ds \\
&+\int_0^{\mu_1} \big((\mathcal{R}(\mu_2)-\mathcal{R}(s))^{\delta+\tau-1} - (\mathcal{R}(\mu_1)-\mathcal{R}(s))^{\delta+\tau-1}\big)\mathcal{R}'(s)ds\| \\
&+\big\|\mathcal{B}\big(\mu_2,\mathcal{H}(\mu_2),\mathcal{G}\mathcal{H}(\mu_2),\mathcal{U}\mathcal{H}(\mu_2)\big) - \mathcal{B}\big(\mu_1,\mathcal{H}(\mu_1),\mathcal{G}\mathcal{H}(\mu_1),\mathcal{U}\mathcal{H}(\mu_1)\big)\big\|
\end{aligned}$$

$$\begin{aligned}
&\leq \frac{\Big(\hat{L}_y + \bar{L}_y\Theta(1+\mathcal{G}^*+\mathcal{U}^*)\Big)}{\rho^{\delta+\tau}\Gamma(\delta+\tau+1)}\big\|(\mathcal{R}(\mu_2)-\mathcal{R}(0))^{\delta+\tau} - (\mathcal{R}(\mu_1)-\mathcal{R}(0))^{\delta+\tau}\big\| \\
&+\big\|\mathcal{B}\big(\mu_2,\mathcal{H}(\mu_2),\mathcal{G}\mathcal{H}(\mu_2),\mathcal{Z}\mathcal{H}(\mu_2)\big) - \mathcal{B}\big(\mu_1,\mathcal{H}(\mu_1),\mathcal{G}\mathcal{H}(\mu_1),\mathcal{U}\mathcal{H}(\mu_1)\big)\big\|
\end{aligned}$$

By using the continuity of the functions $\mathcal{B},\mathcal{R},\mathcal{H}$, and by Lebesgue dominated convergence theorem, from the above inequality, we get $\|(\mathcal{W}\mathcal{H})(\mu_2)-(\mathcal{W}\mathcal{H})(\mu_1)\|\to 0$ as $\mu_1\to\mu_2$. Hence, the operator $\mathcal{W}$ is equicontinuous. From (ii) and (iii), and by the Arzela-Ascoli theorem, it follows that $\mathcal{W}(\mathcal{S})$ is relatively compact. Moreover, since $\mathcal{W}(\mathcal{S})$ is continuous, it is completely continuous. From Theorem 3.1, the operator $\mathcal{P}$ has at least one fixed point in $\mathcal{S}$. Therefore, the system (1) has at least one solution $\mathcal{H}\in C(\chi,\mathcal{X})$.

We then go on to show that the solution to the system (1) is unique. This results in the subsequent theorem.

Theorem 3.3. Let assumptions $(A_1)-(A_3)$ hold. Then the system (1) has a unique solution $\mathcal{H}\in C(\chi,\mathcal{X})$ provided that

$$\Lambda=\frac{(\mathcal{R}(b)-\mathcal{R}(0))^{\delta}}{\Omega_{\mathcal{R}}^{\delta}(b,0)}K_{\varphi}+M_{\mathcal{B}}(1+\mathcal{G}^{*}+\mathcal{Z}^{*})+\frac{(\mathcal{R}(b)-\mathcal{R}(0))^{\delta+\tau}}{\rho^{\delta+\tau}\Gamma(\delta+\tau+1)}L_{\mathcal{F}}(1+\mathcal{G}^{*}+\mathcal{Z}^{*})<1$$

Proof. Suppose that (12) provides the operator 9. Using the same justifications as in Step 1, we have that $\mathcal{P}(\mathcal{S})\subset\mathcal{S}$, where $\mathcal{S}=\{\mathcal{H}\in\mathcal{Q}:\|\mathcal{H}\|\le\Theta\}$, and Θ satisfied (10). Let $\mu\in[0,b],\mathcal{H},v\in\mathcal{S}$, by using the assumptions $(A_1)(i),(A_2)(i)$, and $(A_3)(i)$, we have

$$\begin{aligned}
&\|\mathcal{P}\mathcal{H}(\mu)-\mathcal{P}_{v}(\mu)\|\\
&=\|\frac{\Omega_{\mathcal{Z}}^{\delta}(\mu,0)\varphi(\mathcal{H})}{\Omega_{\mathcal{Z}}^{\delta}(b,0)}+\frac{1}{\rho^{\delta+\tau}\Gamma(\delta+\tau)}\\
&\times\int_{0}^{\mu}\Omega_{\mathcal{H}}^{\delta+\tau-1}(\mu,s)\mathcal{H}'(s)\mathcal{F}(s,\mathcal{H}(s),\mathcal{G}\mathcal{H}(s),\mathcal{Z}\mathcal{H}(s))ds+\mathcal{H}(\mu,\mathcal{H}(\mu),\mathcal{G}\mathcal{H}(\mu),\mathcal{U}\mathcal{H}(\mu))\\
&-\frac{\Omega_{\mathcal{Z}}^{\delta}(\mu,0)\varphi(v)}{\Omega_{\mathcal{Z}}^{\delta}(b,0)}-\frac{1}{\rho^{\delta+\tau}\Gamma(\delta+\tau)}\\
&\times\int_{0}^{\mu}\Omega_{\mathcal{R}}^{\delta+\tau-1}(\mu,s)\mathcal{W}'(s)\mathcal{F}(s,v(s),\mathcal{G}v(s),\mathcal{Z}v(s))ds-\mathcal{B}(\mu,v(\mu),\mathcal{G}v(\mu),\mathcal{Z}v(\mu))\|\\
&\le\frac{(\mathcal{R}(b)-\mathcal{R}(0))^{\delta}}{\Omega_{\mathcal{Z}}^{\delta}(b,0)}\|\varphi(\mathcal{H})-\varphi(v)\|+\|\mathcal{B}(\mu,\mathcal{H}(\mu),\mathcal{G}\mathcal{H}(\mu),\mathcal{Z}\mathcal{H}(\mu))-\mathcal{B}(\mu,v(\mu),\mathcal{G}v(\mu),\mathcal{Z}v(\mu))\|\\
&+\frac{1}{\rho^{\delta+\tau}\Gamma(\delta+\tau)}\\
&\times\int_{0}^{\mu}(\mathcal{R}(\mu)-\mathcal{R}(s))^{\delta+\tau-1}\mathcal{B}'(s)\|\mathcal{F}(s,\mathcal{H}(s),\mathcal{G}\mathcal{H}(s),\mathcal{Z}\mathcal{H}(s))-\mathcal{F}(s,v(s),\mathcal{G}v(s),\mathcal{Z}v(s))\|ds\\
&\le\frac{(\mathcal{R}(b)-\mathcal{R}(0))^{\delta}K_{\varphi}}{\Omega_{\mathcal{R}}^{\delta}(b,0)}\|\mathcal{H}-v\|+M_{\mathcal{A}}\left[\|\mathcal{H}-v\|+\int_{0}^{s}\|\Pi(s,t)\|\|\mathcal{H}-v\|dt+\int_{0}^{T}\|\Pi_{1}(s,t)\|\|\mathcal{H}-v\|dt\right]\\
&+\frac{L_{s}}{\rho^{\delta+\tau}\Gamma(\delta+\tau)}\int_{0}^{\mu}(\mathcal{B}(\mu)-\mathcal{B}(s))^{\delta+\tau-1}\mathcal{R}'(s)\\
&\times\left[\|\mathcal{H}-v\|+\int_{0}^{s}\|\Pi(s,t)\|\|\mathcal{H}-v\|dt+\int_{0}^{T}\|\Pi_{1}(s,t)\|\|\mathcal{H}-v\|dt\right]ds\\
&\le\left(\frac{(\mathcal{R}(b)-\mathcal{R}(0))^{\delta}}{\Omega_{\mathcal{Z}}^{\delta}(b,0)}K_{\varphi}+M_{\mathcal{A}}(1+\mathcal{G}^{*}+\mathcal{Z}^{*})+\frac{(\mathcal{E}(b)-\mathcal{R}(0))^{\delta+\tau}}{\rho^{\delta+\tau}\Gamma(\delta+\tau+1)}L_{\mathcal{S}}(1+\mathcal{G}^{*}+\mathcal{Z}^{*})\right)\|\mathcal{H}-v\|\\
&=\Lambda\|\mathcal{H}-v\|.
\end{aligned}$$

In accordance with condition (14), $\mathcal{P}$ is a contraction. Because of this, $\mathcal{P}$ has a unique fixed point $\mathcal{H}\in C(\chi,\mathcal{X})$, which is the only solution to the system (1) in $C(\chi,\mathcal{X})$.

4. Applications

A real-world example is presented in this section to demonstrate how our key findings can be used.

Example 1. We examine the subsequent nonlinear GCFV-FIDE:

$$\begin{cases} {}_{\frac{1}{2}}^{C}D_{0^+}^{\frac{3}{2},\mu}\left({}_{\frac{1}{2}}^{C}D_{0^+}^{\frac{1}{2},\mu}\left(\mathcal{H}(\mu)-\frac{\mu^2}{8}\left(1+\frac{|\mathcal{H}^e(\mu)|}{2(1+|\mathcal{H}^2(\mu)|)}\right)+\frac{1}{(\mu+4)^2}\mathcal{GH}(\mu)+\frac{1}{2(e^\mu+2)^3}\mathcal{UH}(\mu)\right)\right) \\ =\frac{\mu^2}{2}\left(e^\mu+\frac{\chi}{16(\mu^2+2)}\frac{|\mathcal{H}^e(\mu)|}{(1+|\mathcal{H}(\mu)|)}\right)+\frac{\chi}{64}\mathcal{GH}(\mu)+\frac{\mu^2}{2}\frac{\chi}{32}\mathcal{UH}(\mu), \mu\in\chi=[0,1] \\ \left(\mathcal{H}(\mu)-\frac{\mu^2}{8}\left(1+\frac{|\mathcal{H}(\mu)|}{2(1+|\mathcal{H}^2(\mu)|)}\right)+\frac{1}{(\mu+4)^2}\mathcal{GH}(\mu)+\frac{1}{2(e^\mu+2)^3}\mathcal{UH}(\mu)\right)_{\mu=0}=u_0\in\mathbb{R} \\ \left(\mathcal{H}(\mu)-\frac{\mu^2}{8}\left(1+\frac{|\mathcal{H}(\mu)|}{2(1+|\mathcal{H}^2(\mu)|)}\right)+\frac{1}{(\mu+4)^2}\mathcal{GH}(\mu)+\frac{1}{2(e^\mu+2)^3}\mathcal{UH}(\mu)\right)_{\mu=0}=0 \\ \left(\mathcal{H}(\mu)-\frac{\mu^2}{8}\left(1+\frac{|\mathcal{H}(\mu)|}{2(1+|\mathcal{H}(\mu)|)}\right)+\frac{1}{(\mu+4)^2}\mathcal{GH}(\mu)+\frac{1}{2(e^\mu+2)^3}\mathcal{UH}(\mu)\right)_{\mu=1}+\frac{\left|\mathcal{H}^2\left(\frac{1}{2}\right)\right|}{9\left(1+\left|\mathcal{H}\left(\frac{1}{2}\right)\right|\right)}+\frac{3}{17}=u_1\in\mathbb{R}, \end{cases}$$

where $\tau=\frac{3}{2},\rho=\delta=\frac{1}{2},\mathcal{R}(\mu)=\mu,$

$$\mathcal{F}(\mu,\mathcal{H}(\mu),\mathcal{GH}(\mu),\mathcal{ZH}(\mu))=\frac{\mu^2}{2}\left(e^\mu+\frac{\chi}{16(\mu^2+2)}\frac{|\mathcal{H}(\mu)|}{(1+|\mathcal{H}(\mu)|)}\right)+\frac{\chi}{64}\mathcal{GH}(\mu)+\frac{\mu^2}{2}\frac{\chi}{32}\mathcal{ZH}(\mu),$$

$$\mathcal{B}(\mu,\mathcal{H}(\mu),\mathcal{GH}(\mu),\mathcal{ZH}(\mu))=\frac{\mu^2}{8}\left(1+\frac{|\mathcal{H}(\mu)|}{2(1+|\mathcal{H}(\mu)|)}\right)+\frac{1}{(\mu+4)^2}\mathcal{GH}(\mu)+\frac{1}{2(e^\mu+2)^3}\mathcal{ZH}(\mu),$$

$$\varphi(\mathcal{H})=\frac{\left|\mathcal{H}\left(\frac{1}{2}\right)\right|}{9\left(1+\left|\mathcal{H}\left(\frac{1}{2}\right)\right|\right)}+\frac{3}{17},$$

and

$$\mathcal{GH}(\mu)=\int_0^\mu \mu^2 e^s|\mathcal{H}(s)|ds$$

$$\mathcal{UH}(\mu)=\int_0^1 \frac{s}{\mu^2+3}|\mathcal{H}(s)|ds$$

$$\mathcal{G}^*=\max_{\mu\in[0,1]}\int_0^\mu \mu^2 e^s ds=e-1\approx 1.718$$

$$\mathcal{U}^*=\max_{\mu\in[0,1]}\int_0^1 \frac{s}{\mu^2+3}ds=\frac{e^2-1}{6}\approx 1.065.$$

Let's first verify the hypotheses $(A_1),(A_2)$, and $(A_3).\forall\mu\in[0,1]$ and $v,w,m\in\mathbb{R}$, we get

$$\begin{aligned} &\|\mathcal{F}(\mu,v,\mathcal{G}v,\mathcal{Z}v)-\mathcal{F}(\mu,w,\mathcal{G}w,\mathcal{Z}w)\| \\ &\leq\frac{\mu^2}{2}\frac{\chi}{16(\mu^2+2)}\frac{\|v-w\|}{(1+\|v\|)(1+\|w\|)}+\frac{\chi}{64}\|\mathcal{G}v-\mathcal{G}w\|+\frac{\mu^2}{2}\frac{\chi}{32}\|\mathcal{Z}v-\mathcal{Z}w\| \\ &\leq\frac{\chi}{64}[\|v-w\|+\|\mathcal{G}v-\mathcal{G}w\|]. \\ \|\mathcal{F}(\mu,v,\mathcal{G}v,\mathcal{Z}v)\|&=\left\|\frac{\mu^2}{2}\left(e^\mu+\frac{\chi}{16(\mu^2+2)}\frac{|v|}{(1+|v|)}\right)+\frac{\chi}{64}\mathcal{G}v+\frac{\mu^2}{2}\frac{\chi}{32}\mathcal{Z}v\right\| \\ &\leq\frac{e}{2}+\frac{\chi}{64}[\|v\|+\|\mathcal{G}v\|+\|\mathcal{Z}v\|]. \end{aligned}$$

Hence, hypotheses (A_1) holds with $L_{\mathcal{F}}=\bar{L}_{\mathcal{F}}=\frac{\chi}{64}$ and $\hat{L}_{\mathcal{F}}=\frac{e}{2}$. We get

$$\|\mathcal{B}(\mu,v,\mathcal{G}v,\mathcal{Z}v)-\mathcal{B}(\mu,w,\mathcal{G}w,\mathcal{Z}w)\|$$
$$\leq \frac{\mu^2}{16}\frac{\|v-w\|}{(1+\|v\|)(1+\|w\|)}+\frac{1}{(\mu+4)^2)}\|\mathcal{G}v-\mathcal{G}w\|+\frac{1}{2(e^{\mu}+2)^3}\|\mathcal{Z}v-\mathcal{Z}w\|$$
$$\leq \frac{1}{16}[\|v-w\|+\|\mathcal{G}v-\mathcal{G}w\|+\|\mathcal{Z}v-\mathcal{Z}w\|].$$
$$\|\mathcal{B}(\mu,v,\mathcal{G}v)\|=\left\|\frac{\mu^2}{8}\left(1+\frac{|v|}{2(1+|v|)}\right)+\frac{1}{(\mu+4)^2}\mathcal{G}v+\frac{1}{2(e^{\mu}+2)^3}\mathcal{Z}v\right\|$$
$$\leq \frac{1}{8}+\frac{1}{16}[\|v\|+\|\mathcal{G}v\|+\|\mathcal{Z}v\|].$$

Then, hypotheses (A_2) holds with $M_{\mathcal{B}}=\bar{M}_{\mathcal{B}}=\frac{1}{16}$ and $\hat{M}_{\mathcal{B}}=\frac{1}{8}$. We get

$$\|\varphi(v)-\varphi(w)\|\leq\frac{1}{9}\frac{\|v-w\|}{(1+\|v\|)(1+\|w\|)}\leq\frac{1}{9}\|v-w\|$$
$$\|\varphi(v)\|=\left\|\frac{|v|}{9(1+|v|)}+\frac{3}{17}\right\|\leq\frac{3}{17}+\frac{1}{9}\|v\|$$

Then, hypotheses (A_3) holds with $K_{\varphi}=\bar{K}_{\varphi}=\frac{1}{9}$ and $\hat{K}_{\varphi}=\frac{3}{17}$. Condition (11) also holds:

$$\frac{(\mathcal{R}(1)-\mathcal{R}(0)))^{\delta}}{\Omega_{\mathcal{R}}^{\delta}(1,0)}K_{\varphi}=\frac{1}{e^{-1}}\frac{1}{9}\approx 0.302<1$$

There is at least one solution to the nonlinear system (15) with $\mathcal{H}\in C(\chi,\mathbb{R})$. The following is the uniqueness of the solution to the nonlinear system (15) based on condition (14):

$$\Lambda=\frac{(\mathcal{R}(1)-\mathcal{R}(0))^{\delta}}{\Omega_{\mathcal{G}}^{\delta}(1,0)}K_{\varphi}+M_{\mathcal{G}}(1+\mathcal{G}^*+\mathcal{Z}^*)+\frac{(\mathcal{R}(1)-\mathcal{R}(0))^{\delta+\tau}}{\rho^{\delta+\tau}\Gamma(\delta+\tau+1)}L_{\mathcal{Y}}(1+\mathcal{G}^*+\mathcal{Z}^*)$$
$$=\frac{1}{e^{-1}}\frac{1}{9}+\frac{3.783}{16}+\frac{1}{\frac{1}{4}\Gamma(3)}\frac{\chi}{64}3.783\approx 0.90987<1$$

This implies that the nonlinear system (15) has one solution with $\mathcal{H}\in C(\chi,\mathbb{R})$.

References:

E.Y. Salah, B. Sontakke, A.A. Hamoud, H. Emadifar, A. Kumar, A fractal–fractional order modeling

approach to understanding stem cell-chemotherapy combinations for cancer, Scientific Reports15 (1), 3465 (2025).

A.A. Sharif, A.A. Hamoud, M. M. Hamood and K.P. Ghadle, On New Uniqueness Results for

Riemann-Liouville Fractional Volterra-Fredholm Integro-Differential Equations with Deviating Arguments, DCDIS: Dynamics of Continuous, Discrete and Impulsive Systems, 2025, 25-40.

S.M. Atshan, A.A. Hamoud, Eexistence results for boundary value problems of Volterra-Fredholm systems involving Caputo derivatives, Nonlinear Functional Analysis and Applications, 2024, 545-558.

A. Atangana, D. Baleanu, New fractional derivative with non-local and non-singular kernel, Therm. Sci. 20 (2016) 757.

T.A. Burton, Fixed-point theorem of Krasnoselskii, Appl. Math. Lett. 11 (1998) 85-88.

M. Bohner, S. Hristova, Stability for generalized Caputo proportional fractional delay integrodifferential equations, Bound. Value Probl. 2022 (2022) 14.

M. Caputo, M. Fabrizio, A new definition of fractional derivative without singular kernel, Prog. Fract. Differ. Appl. 1 (2015) 73–85.

S.A. David, J.L. Linares, E.M.D.J.A. Pallone, Fractional order calculus: historical apologia, basic concepts and some applications, Rev. Bras. Ensino Fis. 33 (2011) 4302–4302.

R. Gorenflo, F. Mainardi, Fractional Calculus: Integral and Differential Equations of Fractional Order, Springer Vienna, 1997 [10] K. Hilal, A. Kajouni, S. Zerbib, Hybrid fractional differential equation with nonlocal and impulsive conditions, Filomat 37 (2023) 3291–3303.

F. Jarad, T. Abdeljawad, D. Baleanu, On the generalized fractional derivatives and their Caputo modification J. Nonlinear Sci. Appl. 10 (2017) 2607–2619.

F. Jarad, T. Abdeljawad, Z. Hammouch, On a class of ordinary differential equations in the frame of Atangana-Baleanu fractional derivative, Chaos Solit. Fractals 117 (2018) 16–20.

F. Jarad, T. Abdeljawad, S. Rashid, Z. Hammouch, More properties of the proportional fractional integrals and derivatives of a function with respect to another function, Adv. Differ. Equ. 2020 (220) 303.

F. Jarad, M.A. Alqudah, T. Abdeljawad, On more general forms of proportional fractional operators, Open Math. 18 (2020) 167–176.

I. Mallah, I. Ahmed, A. Akgul, F. Jarad, S. Alha, On ψ-Hilfer generalized proportional fractional operators, AIMS Math. 7 (2021) 82–103.

M. Mebrat, G.M.N. Guerekata, A Cauchy problem for some fractional differential equation via deformable derivatives J. Nonlinear Evol. Equ. Appl. 4 (2020) 55–63.

U.N. Katugampola, New approach to generalized fractional integral, Appl. Math. Comput. 218 (2011) 860-865.

U.N. Katugampola, A new approach to generalized fractional derivatives, Bull. Math. Anal. Appl. 6 (2014) 1–15.

I. Podlubny, Matrix approach to discrete fractional calculus, Fract. Calc. Appl. Anal. 3 (2000) 359–386.

K. Shah, M.A. Alqudah, F. Jarad, T. Abdeljawad, Semi-analytical study of pine wilt disease model with convex rate under Caputo-Fabrizio fractional order derivative,Chaos Solit. Fractals 135 (2020) 109754.

A. Rahmani, W.S. Du, M.T. Khalladi, M. Kostic, D. Velinov, Proportional Caputo Fractional Differential Inclusions in Banach Spaces, Symmetry 14 (2022) 1941.

S.Z. Rida, A.M.A. El-Sayed, A.A.M. Arafa, Effect of bacterial memory dependent growth by using fractional derivatives reaction-diffusion chemotactic model, J. Stat. Phys. 140 (2010) 797–811.

H.G. Sun, W. Chen, H. Wei, Y.Q. Chen, A comparative study of constant-order and variableorder fractional models in characterizing memory property of systems, Eur. Phys. J. Spec. Top. 193 (2011) 185–192.

R. Sreedharan, S.R. Balachandar, R. Udhayakumar, S. Etemad, I. Avc, S. Rezapour, On the fractional perturbed neutral integro-differential systems via deformable derivatives: an existence study, Bound. Value Probl. 2024 (2024) 74.

M. Yavuz, N. Ozdemir, Comparing the new fractional derivative operators involving exponential and Mittag-Leffler kernel, Discrete Contin. Dyn. Syst. 13 (2020) 995–1006.

M. Yavuz, N. Ozdemir, European vanilla option pricing model of fractional order without singular kernel, Fractal Fract. 2 (2018) 3.

S. Zerbib, N. Chefnaj, K. Hilal, A. Kajouni, Study of p-Laplacian hybrid fractional differential equations involving the generalized Caputo proportional fractional derivative, Comput. Methods. Differ Equ., 2024, https://doi.org/10.22034/cmde.2024.61552.2665.

S. Zerbib, K. Hilal, A. Kajouni, Some new existence results on the hybrid fractional differential equation with variable order derivative, Results Nonlinear Anal. 6 (2023) 34–48.

Control Local Scour around Piers and Abutments Using Collars and Bed Sill

Fatima Muhi Mukheef [1]

Ali Adel Zuhaira [2]

Abstract:

Local scour refers to the process of sediment removal around bridge foundations and is among the most serious threats to the stability and safety of bridges. Local scour occurs near piers and abutments due to accelerated flow and downstream vortices and can compromise structural integrity if left unaddressed. Researchers have also recommended employing a ramp (or even a wall) as an engineered flow-altering and controlling strategy to limit scour effects. Previous studies suggested using a collar with a width three to four times the pier diameter or 0.6 times the abutment width, which reduces local scour by disrupting the horseshoe vortices that form at the bases of piers and abutments. Based on these recommendations, the present study incorporated the collar system and modified it with a bed sill, thereby designing a dual countermeasure system to enhance scour resistance. Laboratory tests were conducted with cylindrical piers of varying dimensions and rectangular abutments in a recirculating flume. The experimental results demonstrated substantial performance improvement, with scour depth reduced by over 67.9% around bridge piers and approximately 59.4% around abutments. This combined configuration proved highly effective in controlling local erosion, improving flow stability near the foundation, and ensuring greater structural safety under clear-water conditions. Additionally, the study evaluated the effects of pier and abutment size, flow intensity, bed sill dimensions, and collar size on scour depth using controlled flume experiments. The data were used to develop new non-dimensional empirical equations for predicting scour depth, with a high coefficient of determination ($R^2 = 0.95$), indicating strong model accuracy and reliability.

Keywords: *Local Scour, Bed Sill, Collar, Bridge Pier, Bridge Abutment*.

http://dx.doi.org/10.47832/EngConf3-2

[1] Researcher. AL-Mussaib Technical College, AL-Furat Al-Awsat Technical University, Iraq
fatima.muhi.tcm75@student.atu.edu.iq

[2] Researcher. AL-Mussaib Technical College, AL-Furat Al-Awsat Technical University, Iraq
aliadelalzuhairi@atu.edu.iq

1. Introduction

Bridges are important components of today's transportation system. They provide an acceptable margin of safety and expedient travel from one side of a river to the other, across valleys and other barriers to transportation. However, without a doubt, scour, the removal of soil around bridge foundations by flowing water, is one of the most serious hazards to our bridge structures. As shown in Figure 1, local scour (scour near piers and abutments) is the most severe because the water has gained velocity. When the water encounters a pier or abutment, vortex motion is created, which can potentially scour the soil around a bridge foundation severely.[1]. Scour can expose foundation elements, reduce bearing capacity, and, in extreme cases, cause total catastrophic bridge failure [2].

Fig.1 Local scour around the foundation bridge

The investigation of local scour depends on interrelated factors such as flow velocity, sediment size, pier geometry, and flow depth [3-4]. When hydraulic conditions change during flood events, the threat of scour increases significantly, requiring attention to the hydraulic design and maintenance of bridge foundations. In addition to increased hydraulic conditions, climate change has dramatically increased rainfall and the magnitude of flooding events [5]. Predicting and limiting scour and scour depth under bridges is critical.

To improve our understanding of scour development mechanisms, it is necessary to differentiate between clear-water scour (CWS) and live-bed scour (LBS) conditions, as shown in Figure 2.

Clear-water scour occurs when the flow velocity in the approach flow exceeds the threshold for sediment motion around the pier. Still, the upstream bed material is mainly stationary, resulting in little or no incoming sediment supply to replace the sediment flow. Ultimately, scour will continue until a dynamic equilibrium is achieved where the bed shear stress is below the required value of bed shear stress to begin sediment entrainment within the scour hole [1,4].

Nonetheless, live-bed scour happens when the flow velocity is sufficiently high to set bed sediment in motion within the approach flow. This sediment can be consistently carried toward the pier, where a complex scour and deposition process occurs inside the scour hole

[3,5]. As sediment transport is continuous, the depth and rate of scour will be modified to a more dynamic equilibrium state with the supplied sediment (HEC-RAS, 2023; National Academies, 2021).

It is important to ascertain whether the environmental conditions are conducive to clear-water or live-bed scour before one can realistically predict or model scour depth. In other words, scour holes typically develop to a greater depth under clear-water scour conditions and stabilize, since the sediments are not being supplied from the channel bed or bank. Conversely, live-bed conditions have moving sediment, which can easily refill or reform a scour hole, resulting in less maximum scour depth [4,1]. This is important in differentiating the use of designs and countermeasures.

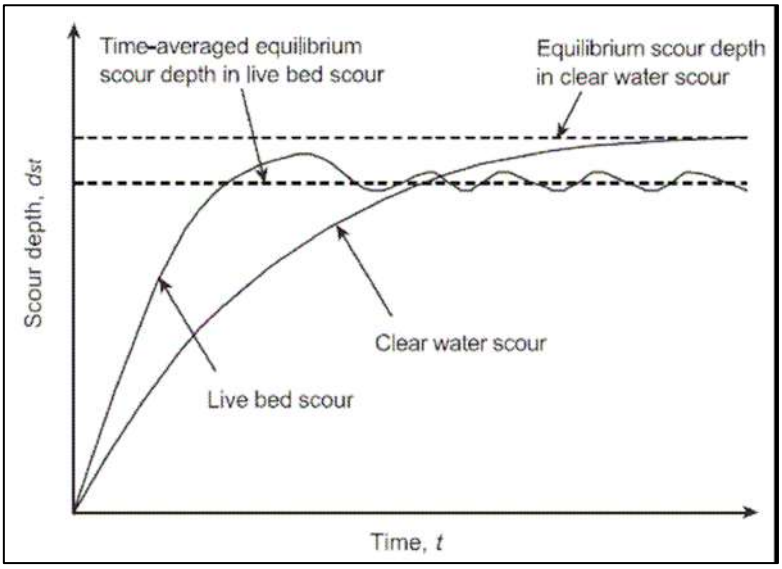

Fig.2. Clear water scour and live bed scour

Engineers have created numerous countermeasures and design methods to reduce scour, and, generally, they will achieve a reduced scour depth or increased strength and stability of the foundation. Examples include riprap, collars, and submerged vanes, which all impact the flow field and affect the duration and intensity of the vortices [6-7]. The factors leading to the selection of countermeasures, such as location, availability of materials, and hydraulic considerations, can vary from site to site. Researchers are working to improve upon existing countermeasures or create new countermeasures that are sustainable, cost-effective, and minimize negative environmental impacts while still promoting security [8].

In summary, understanding the relationship between hydrodynamic conditions and sediment mobility, especially during the transition from clear-water to live-bed scour, is an essential step towards improving the state of practice in the robustness and confidence of bridge foundations under shifting flow and climate conditions.

Even though numerous research works have been done on scour countermeasures, the majority of the studies have concentrated on the effectiveness of various individual protection methods, like riprap, collars, and bed sills, on their own. However, little emphasis has been put on the combined effect of various countermeasures and their potential to increase the effectiveness of scour protection. The combined effect of collars and bed sills in clear water

scour has not been fully explored. The present study, therefore, aims to investigate the effectiveness of the combined effect of collars and bed sills in reducing scour in the region of bridge piers and abutments. The study will provide a deeper understanding of how the combined effect of various countermeasures affects the scour depth and flow, thus creating a basis for the development of more efficient and effective scour countermeasures. .

2. Armoring countermeasures

The most common technique for controlling local scour depth is the armoring countermeasures, including riprap and non-traditional armoring structures. By protecting the armor layers and improving the anti-scour properties of the bed materials, the local scour depth is consistently decreased. Shielding countermeasures are also referred to as passive scour countermeasures:

According to Chiew [9] and Van Ballegooy [10], experimental investigations focus on how scour and safety precautions behave around bridge structures under various hydraulic conditions. Chiew's [9] study examines the stability of riprap and local scour at bridge piers in rivers undergoing gradual bed deterioration. The results show that, except for the local area around the pier, the overall riverbed morphology is mostly unaltered. The combination of local pier scours and broad bed degradation results in a total scour depth that stabilizes after about 24 hours. The riprap surrounding the pier develops into a stable mound as degradation advances, as shown in Figure 1, but it may fail during subsequent floods due to massive migratory dunes; this failure mode is known as bed-degradation-induced failure. The use of cable-tied blocks and riprap as scour countermeasures at bridge abutments was also investigated by Van Ballegooy [10]. The study evaluated two abutment types, wing-wall and spill-through. In contrast to riprap aprons, cable-tied block aprons allow the scour hole to form nearer the abutment. Predictive equations were created to determine the ideal apron size and extent necessary to avoid abutment damage since trough formation in live-bed conditions caused the aprons to settle.

All of these studies show that although riprap and related countermeasures can effectively prevent scour, their effectiveness depends heavily on construction type, hydraulic conditions, and long-term bed stability. (Figure 3.)

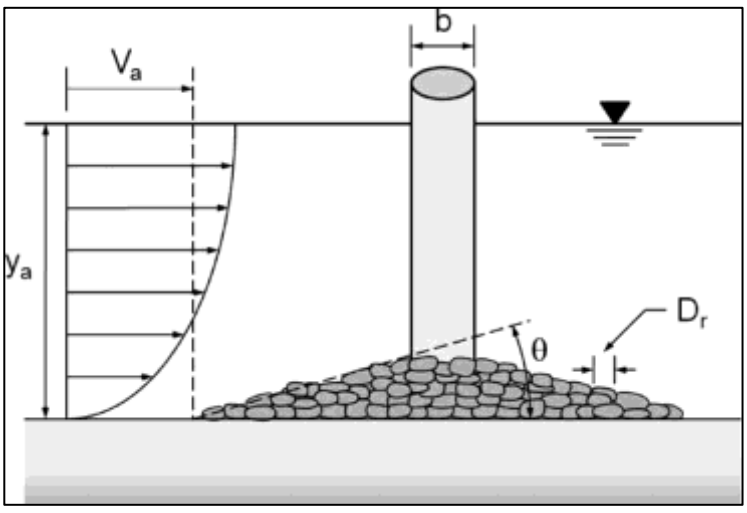

Fig.3 Illustration of the general pier riprap design problem[9].

3. Flow-altering countermeasures

Techniques that are firmly fixed close to bridge piers and abutments to reduce the flow velocity that causes scour are known as flow-altering countermeasures. These consist of helical threading, splitter plates, vanes, slots, collars, and sacrificial piles [10].

3.1. Collars:

A flow-altering device, known as a collar, has been used to protect piers from local scour. According to earlier studies, scour can be significantly reduced by installing a collar on a single pier [11]. Earlier studies on the use of collars to protect piers were conducted by Laursen & Toch[12]. The study found this method effective in minimizing scour around the pier.

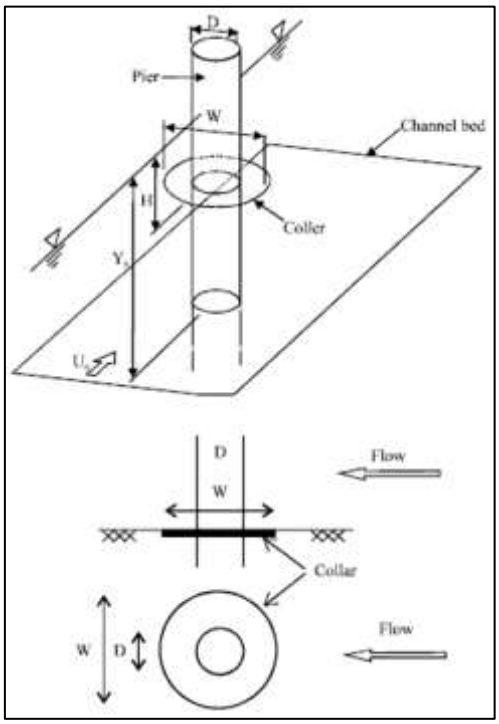

Fig.4 Collars positioned around circular pier[13]

Collars are well-known effective measures for reducing local scour of bridge piers and abutments by modifying near-bed flow directions and preventing the horseshoe or wake vortices that induce sediment movement [14,1]. Experimental studies indicated that for bridge piers, if circular collars were installed with widths of about three to four pier diameters, scour depth could be eliminated or reduced. Chiew [14] reported that no scour would be observed at a collar width of three pier diameters, and Kumar et al.[15] found that a collar with a width of four pier diameters had no scour on the front and sides of the pier; only minor scour occurred behind the pier because of wake vortices.

For bridge abutments, Osroush et al.[16] found that a collar length of approximately 0.6 abutment widths provided optimal performance. Full collars around the abutment provided the most excellent stability by reducing turbulence and flow separation. However, partial collars improved performance and were very cost-effective when adjusted to the abutment geometry.

Gökmener et al [17] have tested semi-circular collars around semi-circular end abutments to assess their effectiveness in reducing local scour under unsteady clear-water flow conditions. A maximum reduction in scour depth of up to 72% was achieved. The semi-circular collars produced better performance than the rectangular ones. The optimal annual averaged design configurations were found when the largest collar was placed at the bed level. Collars were confirmed to affect the reduction of local scour, based on the two categories of scour control collar characteristics, their shape, width, or bed level placement, and these results are important for future studies.

Overall, the installation of collars, used singly or in combination with bed sills, has demonstrated considerable potential as an effective scour control measure, improving the hydraulic stability of bridge foundations across a range of flow conditions.

3.2. Bed Sill:

A bed sill is a passive scour-control method that changes flow patterns. There are two kinds of bed sills: upstream and downstream.

Razi et al. [18] performed laboratory experiments to study bed sills in controlling scour depth at cylinder piers when flowing over in clear water. The experiments took place at a flume with a depth of 0.5 meters, a width of 0.8 m, and a length of 6.0 m, along with sediment bed contours and scour depth. A bed sill was comparable in size to the sand bed, which was considered to be 10 mm thick, 0.15 m high, and 0.6 m long. When the bed foundation is placed upstream of the piers, the amount of erosion depth in front of the piers is drastically reduced. Scour, however, downstream of the piers causes a greater likelihood of degrading the bed surface in this instance than with the bed sill placed downstream. The reason for this lies in the fact that the bed sill will compound general scour downstream of the piers when a foundation is present upstream of the piers. Therefore, the bed sill should be located downstream of the piers at the snap of the piers, in which case, the maximum protection was 29% lower for the piers' scour depth.

Additionally, an experimental study was conducted to investigate the impact of bed sills on local erosion near bridge foundations immersed in cohesive soils. By Ahmadi et al. [19]. The bed sill was positioned downstream at varying distances from the piers. As pier models, cylinder-shaped pipes with diameters of 75 mm and 60 mm were used. The findings indicate that the distance between the bed sill and the piers had a greater influence on reducing scour volume and depth than other parameters. Shortening the bed sill space from the piers decreases both scour depth and volume. The optimal location for bed sill installation is beside the piers. It was also shown that there is no correlation between scour depth and the pier's Froude number.

In a laboratory setting, Sanadgol et al.[20] investigated the effectiveness of bed sills in reducing scour depth at four-sided piers over time. Studies were conducted on rotund-nosed piers with flow velocities just below the sediment motion threshold (V/Vc = 0.95) and width-to-length ratios (L/b) of 1, 2, 3, and 4. The PVC bed sill was as wide as the flume and only one centimeter thick. It was located downstream of the piers at various positions, D, so that

D/b = 0, 1, 2, and 3. It was flat with the bed. It was found that the bed sill of a rectangular pier was significantly less effective than that of a circular one; scour depth and efficiency declined with pier length. The most efficient round-nosed piers were those with L/b = 1, 2, 3, and 4, which were 32.5%, 21.3%, 14.4%, and 5.7%, respectively. Therefore, it is not recommended to apply a bed sill to rotund-nosed rectangular piers to limit local scour when the width-to-length ratio exceeds 2. Furthermore, the bed sill works best when attached to the downstream end of the pier; its effectiveness declines with increasing distance from the pier.

4. Experimental setup

The experiments were carried out in a steel laboratory flume (6.6 m long × 0.4 m wide × 0.4 m deep) with a closed water recirculation system. As shown in Figure 5. The facility includes a 1.0 m inlet tank and a 5.6 m-long working section, divided into three sections, each featuring a sand-filled bed uniformly filled with corrosive material to a depth of 0.10 m throughout its length. The bed was built using non-swelling wood, with a depth of 0.1 m, to stabilize flow between sections.

A circular aluminum tower with three screens prevents debris from entering the flume, and a centrifugal pump draws water from below the flume tank and recirculates it. Flow depth is controlled by the downstream tailgate and measured with a point gauge to an accuracy of ±1 mm. Discharge was calculated with a sharp-crested rectangular weir (0.4 m × 0.25 m).

After each test run, the flume is drained, and the sand bed is leveled to an even depth using a scraper made from a piece of wood attached to vertical strips to ensure an accurate leveling.

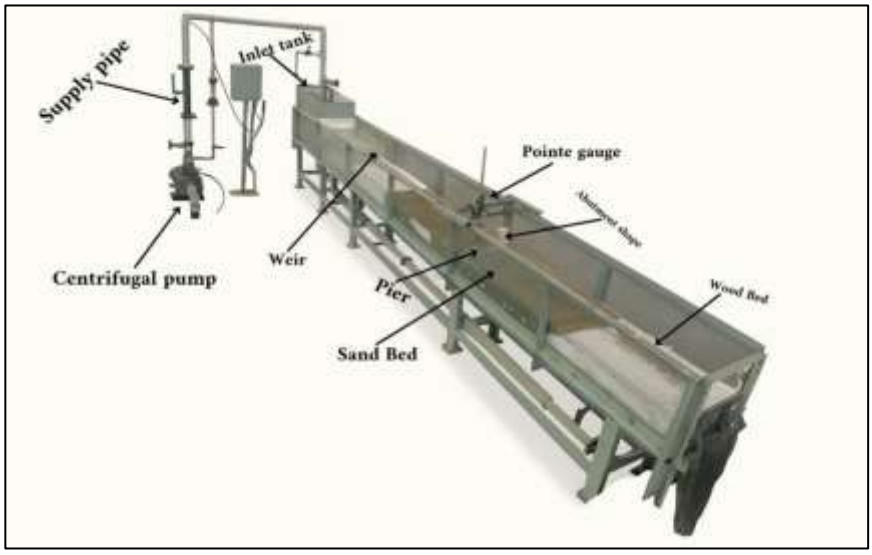

Fig.5 The flume lab.

5. Influence of main parameters

Several factors can influence scour depth, including the pier characteristics and the upstream abutment elevations. This section identifies the primary controlling parameters that affect scour depth. To ensure that all other factors are held constant, each factor is

individually evaluated in a controlled laboratory environment. By solely evaluating one factor in the laboratory environment, the effect of the factor can be isolated, allowing for an unambiguous evaluation of its impact on scour depth.

5.1. Pier size:

The effect of the pier's size on the local scour is significant, as the larger the pier, the deeper the scour hole that is formed upstream, as well as the deposition of the sediment downstream. Such behavior is mainly due to the strength of the horseshoe vortex that is formed at the upstream face of the pier, which increases with the increase in the pier's diameter. Previous studies have confirmed the strong correlation between the pier's diameter and the depth of the scour hole. Therefore, in the current study, various sizes of the pier's diameter, based on the ranges that have been used in previous experimental studies, have been chosen to investigate their effect on the scour. By changing the diameter of the pier while keeping the other parameters as constant as possible, the direct effect of the size of the pier on the formation of scouring can be observed. As shown in Figure 6, the effect of the diameter of the pier is more obvious. In contrast, the effect of the other parameters is minimized in the resulting profiles of the experiment.

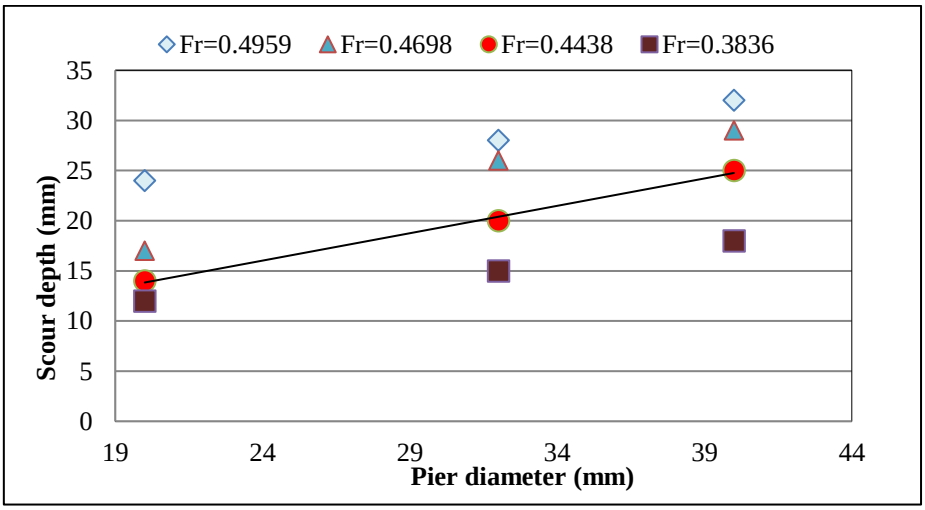

Fig.6 Scour depth development in relation to pier diameter.

5.2. Abutment size:

The transverse dimension of the abutment is seen to have an important role to play in the development of scour holes near bridge abutments. This is because, with an increase in the size of the abutment, the resistance offered by the abutment to the approaching flow will be greater, increasing flow acceleration and, therefore, the development of primary and secondary vortices near the abutment. These vortices will, therefore, increase the bed shear stress, resulting in deeper scour holes.

In the present study, the dimensions of the abutment were varied to assess their effect on the development of scour under similar flow conditions. By changing the transverse length of the abutment and keeping other parameters fixed, the effect of the abutment dimensions on scour characteristics can be easily identified. Figure 7 shows how the abutment with a transverse length of 100 mm and an inner diameter of 40 mm develops a wider and lower

friction zone compared with the abutment with a transverse length of 80 mm, as shown in Figure 7.

In order to understand the influence of abutment dimensions, it is necessary to highlight the importance of designing effective scour protection measures, as the optimization of the geometric configuration of the abutment could contribute to the reduction of the intensity of scour and the stability of the bridge foundations.

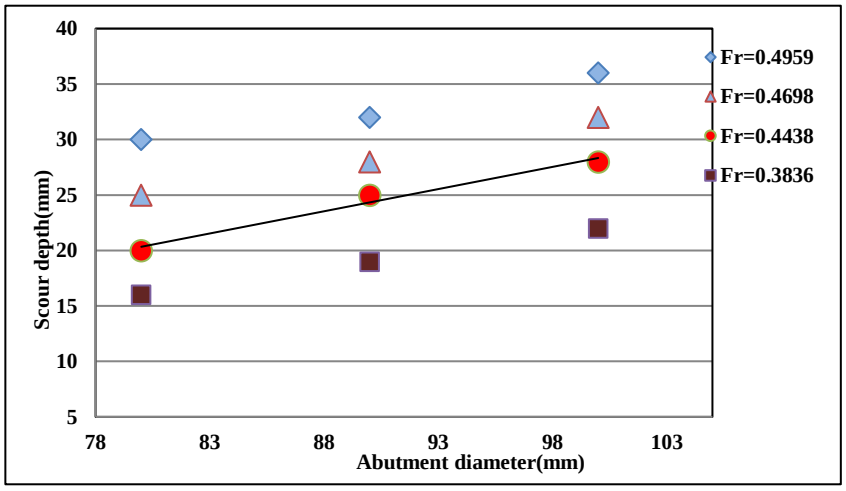

Fig.7 Scour depth development in relation to abutment diameter.

5.3. Flow intensity:

The flow intensity, usually expressed as the ratio between shear velocity and critical velocity for sediment motion, is considered to be one of the most important factors affecting local scour development near hydraulic structures. In clear-water scour, it is assumed that the processes of sediment transport and development of scour holes are controlled by bed shear stress, as opposed to flow depth. In cases where the applied bed shear stress exceeds the threshold required for initiating sediment motion, bed sediments start to be transported and removed from the area surrounding the structure.

The interaction of the incoming flow with the resulting obstruction caused by the pier or the abutment leads to complex three-dimensional flow structures such as the horseshoe vortex and the wake vortex, which increase the local bed shear stress and the rate of sediment entrainment in the scour hole. Even in cases where no additional sediment is provided from the upstream bed, these complex flow structures are known to be capable of displacing the available bed material to increase the scour depth to an equilibrium condition. The results of the experiments conducted in the present study indicate that the depth of local scour increases with the increasing level of flow intensity. As shown in Figures 8 and 9, the depth of local scour increases linearly with the increasing level of shear velocity, especially before

the critical level of sediment mobility is attained. This confirms the dominant role of the level of flow intensity in controlling the formation of scour, especially in clear water.

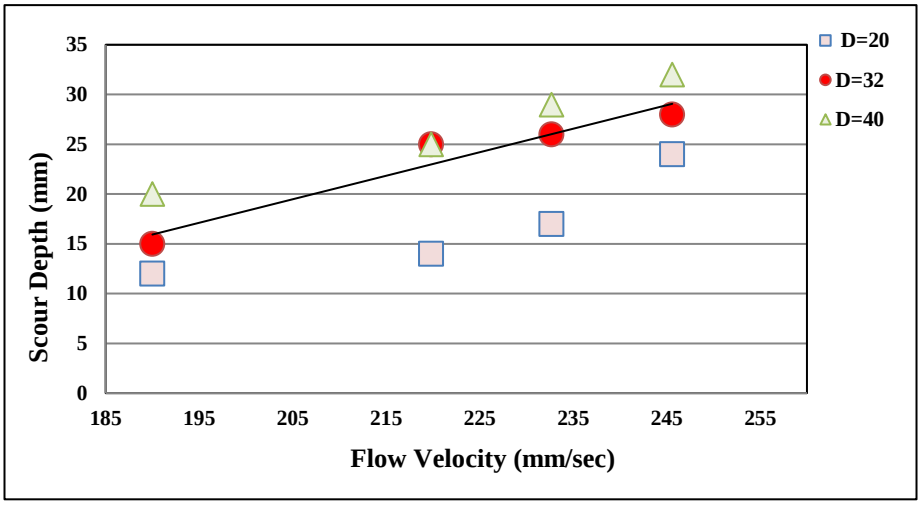

Fig.8 Scour depth development for a pier with flow intensity

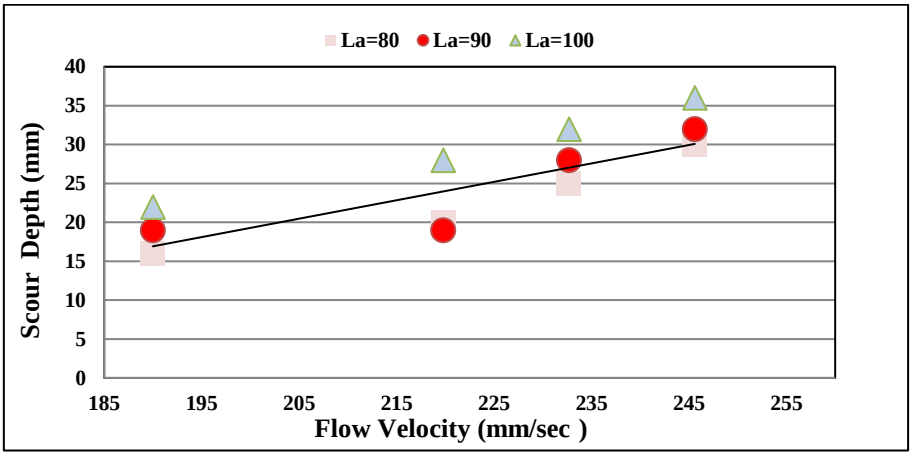

Fig.9 Scour depth development for an abutment with flow intensity

5.4 The bed sill dimension:

Previous research indicated that a bed sill thickness of 24mm was sufficiently effective in reducing scour potential when it was teamed on a pier with a collar. The sill, while it remained a 200mm wide feature, contributed significantly to constraining the local scour immediately behind the pier when used in combination with the collar. Turning to the abutment, bed sills were used at 50, 55, and 60mm widths with consistent thickness to maintain similar collar sizes on each abutment dimension. The results confirmed that the sill-collar combination was effective at controlling the local scouring, and support that the design with shallower, yet wider, sill and collar combination locations would assist with structural safety.

6. Development of a new formula

The scour depth of the pier depends on the variables previously stated. The non-dimensional formula is presented.

$$\left(\frac{ds}{D}\right)_{\text{pier}} = F_4\left\{\left(\frac{T}{D}\right), \left(\frac{W}{D}\right), \left(\frac{y}{D}\right), \left(\frac{vc}{v}\right), \left(\frac{Cw}{D}\right), \left(\frac{Ct}{D}\right), \left(\frac{Ks}{D}\right), Fp\right\}$$

The equation was analyzed using MATLAB via nonlinear regression methods.

$$ds/_D = c_1 \times\{(T/_D)^{c_2} \times (W/_D)^{c_3} \times (vc/_v)^{c_5} \times (Cw/_D)^{c_6} \times (Ct/_D)^{c_7} \times (Ks/_D)^{c_8} \times (Fp)^{c_9}\}$$

This formula's coefficient of determination (R_2) is 0.95. The excellent accuracy of the models is indicated by the R^2 value, which displays a high degree of agreement between the predicted and observed data. Figure 10 shows that a higher R^2 (0.95) accurately captures most of the observed variation.

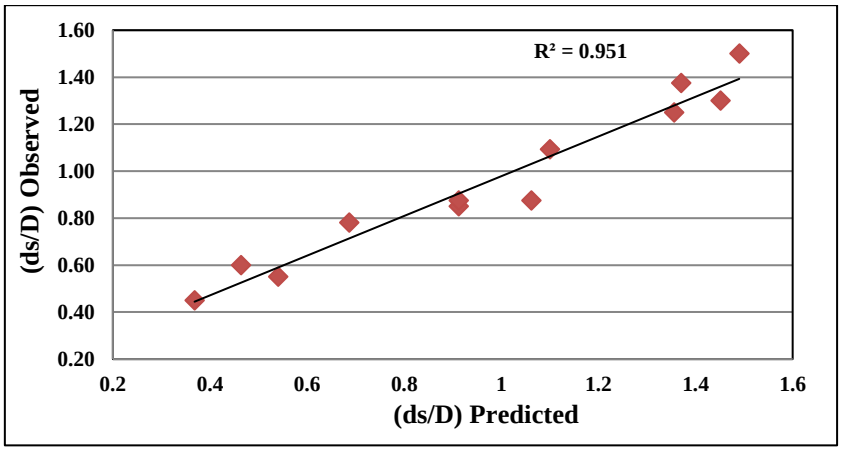

Fig.10 Comparison of Equation Values to Evaluate Result Accuracy

The previously mentioned factors determine the abutment's scour depth. The non-dimensional equation is shown.

$$\left(\frac{ds}{La}\right)_{\text{abutment}} = F_4\left\{\left(\frac{T}{La}\right), \left(\frac{W}{La}\right), \left(\frac{y}{La}\right), \left(\frac{vc}{v}\right), \left(\frac{Cwl}{La}\right), \left(\frac{Ctl}{La}\right), \left(\frac{Ks}{La}\right), FpL\right\}$$

The equation was analyzed using MATLAB via nonlinear regression methods.

$$ds/_{La} = c_1 \times\{(T/_{La})^{c_2} \times (W/_{La})^{c_3} \times (y/_{La})^{c_4} \times (Ks/_{La})^{c_5} \times (Cwl/_{La})^{c_6} \times (Ctl/_{La})^{c_7} \times (vc/_v)^{c_8} \times (Fpl)^{c_9}\}$$

This formula's coefficient of determination (R_2) is 0.92. The excellent accuracy of the models is indicated by the R^2 value, which displays a high degree of agreement between the predicted and observed data. Figure 11 shows that a higher R^2 (0.92) accurately captures most of the observed variation.

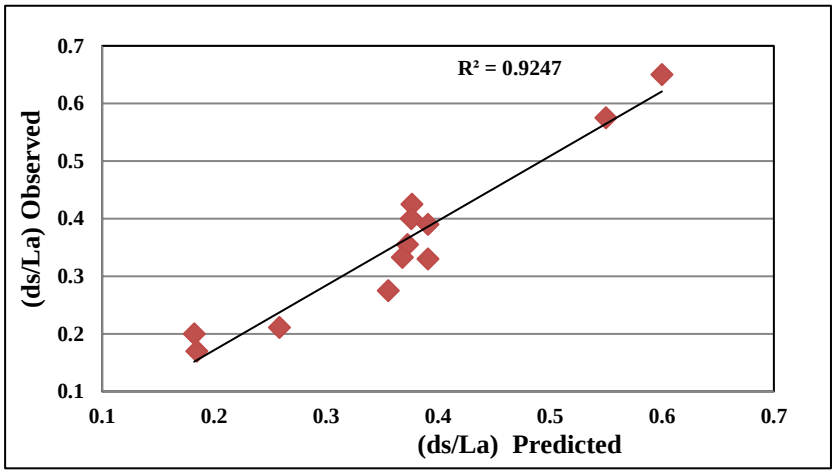

Fig.11 Comparison of Equation Values to Evaluate Result Accuracy.

7. Results

The results of the experiments show that the combined application of the collar and bed sill significantly changes the local flow field around the bridge pier and abutment, resulting in a significant reduction in the scour formation. The collar works as a horizontal obstacle to weaken the downward flow velocity approaching the upstream face of the pier or abutment, hence reducing the intensity of the horseshoe vortex, which is the major scouring mechanism at the bed around the pier foundation. At the same time, the bed sill works as an energy dissipator to reduce the velocity of the flow at the bed and the bed shear stress acting on the sediment particles.

The experimental results revealed that such hydraulic modifications resulted in a notable decrease in the flow velocity around the structures, achieving a reduction of about 67.9% around the pier and 59.4% around the abutment. Consequently, the entrainment of sediments is reduced, and the material on the riverbed around the structures is more stable, resulting in a notable reduction in the depth of scouring. Additionally, when comparing the results with those of a previous study by Khassaf [21], who focused on the application of a bed sill as a single measure, it is evident that the application of collars and bed sills together is more effective, achieving a reduction of more than 65.1% in the depth of scouring around the pier.

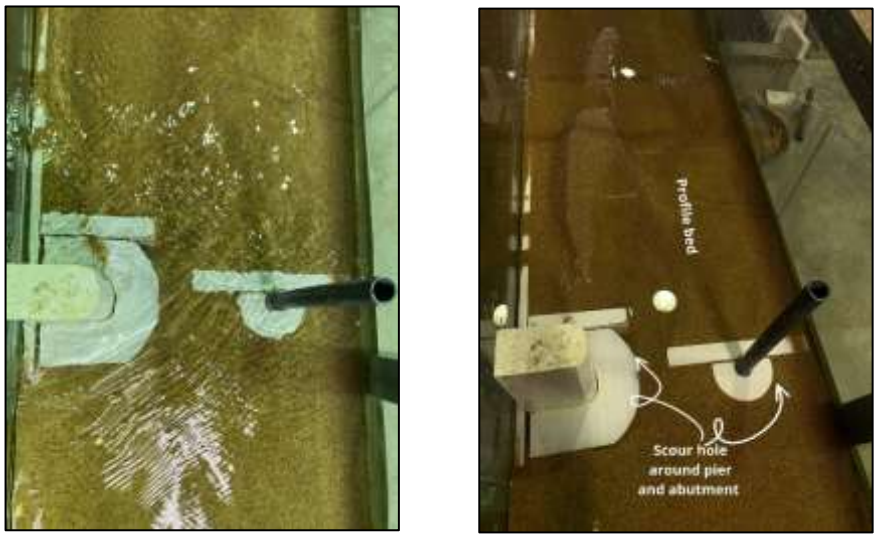

(a) **(b)**

Fig.13 The effect of flow intensity on reducing local scour. (a) During run, (b) after run.

8. Conclusion

This study addressed the problems of local scour caused by the sand grains scouring around the pier and the abutment. Two countermeasures, the collar and bed sill, were investigated and located around the pier and abutment under clear-water conditions. The following conclusions can be made:

1) The bed sill and collar were effective in reducing the maximum scour depth not only by decreasing scour magnitudes overall, but also by shifting the location of maximum scour from the pier and abutment to the collar region.

2) The protective approach was found to provide a reduction in scour at the pier of 67.9% for a given flow velocity of 0.2459m/sec, demonstrating the effectiveness of the approach in reducing scour due to flow velocity

3) The protective measures deployed at the declared flow velocity produced a noticeable decrease in local scour around the bridge abutment with a 59.6% reduction, therefore confirming their high efficiency as a local scour mitigation measure around bridge foundations.

4) The comprehensive design equation, which takes into account all pier parameters, has a coefficient of determination (R^2) of 0.95, whereas the abutment-specific model has an R^2 value of 0.92**.**

Reference:

B. W. Melville and S. E. Coleman, Bridge scour. Water Resources Publication, 2000.

E. V Richardson and S. R. Davis, "Evaluating scour at bridges," United States. Federal Highway Administration. Office of Bridge Technology, 2001.

Y.-M. Chiew and B. W. Melville, "Local scour around bridge piers," J. Hydraul. Res., vol. 25, no. 1, pp. 15–26, 1987.

R. Ettema, "Scour at bridge piers," 1980.

P. F. Lagasse, L. W. Zevenbergen, J. D. Schall, and P. E. Clopper, "Bridge scour and stream instability countermeasures. experience, selection, and design guidance," United States. Federal Highway Administration. Office of Bridge Technology, 2001.

J. Chabert, “Etude des affouillements autour des piles de ponts,” Rep. Natl. Hydraul Lab., Chatou, 1956.

R. V Raikar and S. Dey, "Pier scour and thin layered bed scour within a long contraction," Can. J. Civ. Eng., vol. 33, no. 2, pp. 140–150, 2006.

D. M. Sheppard, M. Odeh, and T. Glasser, "Large scale clear-water local pier scour experiments," J. Hydraul. Eng., vol. 130, no. 10, pp. 957–963, 2004.

D. C. Froehlich, "Protecting bridge piers with loose rock riprap," J. Appl. Water Eng. Res., vol. 1, no. 1, pp. 39–57, 2013.

P. Williams, R. Balachandar, V. Roussinova, and R. Barron, "Particle image velocimetry evaluation of flow-altering countermeasures for local scour around a submerged circular cylinder," Int. J. Sediment Res., vol. 37, no. 4, pp. 411–423, 2022, doi: 10.1016/j.ijsrc.2022.03.001.

M. Heidarpour and H. Afzalimehr, "Local scour protection at bridge piers groups using collar," 한국수자원학회 학술발표회, pp. 1207–1208, 2005.

E. M. Laursen and A. Toch, Scour around bridge piers and abutments, vol. 4. Iowa Highway Research Board Ames, IA, 1956.

M. B. Mashahir, A. R. Zarrati, and E. Mokallaf, "Effect of collar length on time development of scouring around rectangular bridge piers," in Proc., 4th Int. Conf. Scour Erosion, 2008, pp. 252–255.

Y.-M. Chiew, "Scour protection at bridge piers," J. Hydraul. Eng., vol. 118, no. 9, pp. 1260–1269, 1992.

V. Kumar, K. G. R. Raju, and N. Vittal, "Reduction of local scour around bridge piers using slots and collars," J. Hydraul. Eng., vol. 125, no. 12, pp. 1302–1305, 1999.

S. A. Hosseini, M. Osroush, and A. A. Kamanbedast, "Experimental study of the effect of length and width of the partial and full collars on reduction of scouring and sedimentation patterns around bridge abutments," ISH J. Hydraul. Eng., vol. 27, no. sup1, pp. 294–303, 2021.

S. Gökmener, "Effect of flow intensity and collars on scour depths around bridge abutments," 2023, Middle East Technical University (Turkey).

S. Razi, F. Salmasi, A. Hosseinzadeh Dalir, and D. Farsadizaeh, "Application of bed sill to control scouring around cylindrical bridge piers," J. Civ. Eng. Urban., vol. 2, no. 3, pp. 115–121, 2011.

M. M. Ahmadi, M. Hossiennejad, and M. Rahimpour, "Experimental study on effect of downstream bed sill on local scour around bridge piers in cohesive sediment," Irrig. Water Eng., vol. 5, no. 4, pp. 1–15, 2015.

E. Sanadgol, M. Heidarpour, and R. Mohammadpour, "Reduction of local scouring at round-nosed rectangular piers using a downstream bed sill," J. South african Inst. Civ. Eng., vol. 63, no. 3, pp. 62–70, 2021.

S. I. Khassaf, S. A. Yost, and A. A. Abulwahed, "Control of local scour depth around btidge pier using down strem bed sill," Kufa J. Eng., vol. 5, no. 1, pp. 85–104, 2013.

Incorporation of TBCP and ZnO/MgO Nanocomposites to Enhance the Toughness, Thermal Conductivity, and Mechanical Properties of Epoxy

Mariam Thabet Dhyool [1]

Zoalfokkar Kareem Mezaal [2]

Ali Salah Hassan [3]

Abstract:

Epoxy resins are good because they are thermally stable and easy to work with, but they are also brittle and don't let heat escape very well. The following article suggests a dual-modification approach, including i) adding a polyether triblock copolymer to a matrix to increase its toughness at one-to-nine weight percent, and ii) incorporating ceramic nano-fillers using a solution method at 0.5-3 weight percent, such as zinc oxide or magnesium oxide, which will be followed by full-scope mechanical, thermal, and morphology characterization of the resulting systems. The formulation containing 6 wt% TBCP and 3 wt% ZnO delivered the best balance of properties, raising tensile strength by ~30%, elastic modulus by ~25%, and peak fracture toughness by ~75% relative to neat epoxy. Field-emission SEM revealed uniform phase-separated TBCP domains that activate cavitation and localized shear yielding, while well-dispersed ZnO at low–moderate loadings impeded crack propagation; agglomeration at 3 wt% and above correlated with diminishing mechanical returns. Nanofiller composites demonstrate a clear thermal conductivity improvement against neat epoxy and TBCP-only systems with ZnO-filled specimens outperforming MgO for comparable loadings; changes in hardness were subtle for all series. The rubbery toughening approach with additional high-surface-area ceramic channels ensures simultaneous improvements in thermofunctional properties and damage tolerance overall. The results expose the optimal compositional window of 6 wt% TBCP + 3 wt% ZnO composition under coupled mechanical and thermal stresses found was truly narrow, yet nanodielectric filler fractions above this must be dispersed at the nanoscale to be retained, which leads to property deterioration across the higher filler fractions.

Keywords. *Epoxy-based Coating, ZnO Nanofiller, TBCP, MgO Nanoparticles (nano-MgO), Maximum Stress in Tension, Modulus of Elasticity (tension).*

http://dx.doi.org/10.47832/EngConf3-3

[1] Researcher. College of Materials Engineering, University of Babylon, Iraq mariamthabet672@gmail.com

[2] Researcher. College of Materials Engineering, University of Babylon, Iraq mat.zoalfokkar.alobad@uobabylon.edu.iq

[3] Researcher. College of Materials Engineering, University of Babylon, Iraq mat.ali.salah@uobabylon.edu.iq

1. Introduction

Throughout many years, resins made of epoxy have gained significant importance in many industry and everyday situations because they are very resistant to heat characteristics and corrosion properties, exhibit elevated mechanical durability, and stick well to many surfaces [1]. On the other hand, organic coatings, especially epoxy coatings, have limited resistance to both crack initiation and propagation, which leads to lower mechanical strength and localized defects causing aesthetic problems [2]. Despite having many favorable properties for use in applications requiring both high toughness and thermal conductivity, epoxy resins are naturally brittle and have low thermal conductivity (0.1-0.3 W/m·K) and poor mechanical performance [3]. Motor–generators generate significant heat during operation due to friction and energy losses, while their metallic parts are subject to corrosion and degradation under harsh environmental and operational conditions [4]. To address these issues, inorganic fillers with high thermal conductivity are incorporated into the epoxy matrix to enhance heat transfer and improve mechanical properties [5]. Among these fillers, zinc oxide (ZnO) and magnesium oxide (MgO) are commonly used; ZnO, in particular, improves thermal resistance and stability, contributing to increased heat dissipation [6]. Furthermore, the inclusion of nano oxides within the epoxy-based matrix markedly enhances the mechanical, thermal, and corrosion prevention characteristics in relation to the pure material of epoxy, owing to their high area of the surface and layered architecture [7,8]. These particles are the subject of extensive research due to their enhancement of the stability of the thermal and the mechanical characteristics of substances made from polymers [9]. Several studies have improved the toughness of epoxy resin using functionalized rubbers, engineering thermoplastics, and block copolymers. Salam O, et al. used natural rubber (NR) and acrylonitrile butadiene styrene (ABS) to enhance epoxy toughness [10]. Z.A.R.A.H. Saadi et al. showed that liquid silicone rubber (LSR) and a polyurethane-based polyol improved toughness and mechanical properties such as tensile modulus, strength, fracture toughness, and impact strength. Nanomaterials have also been explored to enhance the mechanical and thermal performance of epoxy composites [11]. Naga Raju et al. found that 2 wt.% zinc oxide (ZnO) nanoparticles enhanced hardness and tensile strength [12]. Halder et al. observed that surface-modified ZnO nanoparticles coated with polyvinyl alcohol (PVA) improved dispersion, and at 2 wt.% ZnO, composites showed improvements in mechanical performance [13]. Z.A.R.A.H. Saadi et al. found that a 3 wt.% concentration of TBCP gave the best enhancement in mechanical properties, while tungsten carbide (WC) further increased tensile strength, elastic modulus, and impact strength [14]. Anwar Qasim Saeed et al. studied magnesium oxide, BN, and combination nanoscale particles at different quantities 1,3,5, and 7 weight percent with the epoxy resin material; SEM and FTIR analyses confirmed uniform particle dispersion and improved mechanical properties, notably at 7 wt.%. % BN due to homogeneous distribution and better stress transfer [15].

This study examines the effects of oxide of zinc and magnesium oxide, nano-particles on the thermal, mechanical, and morphological characteristics of coatings made of epoxy at various concentrations of 0.5, 1, 1.5, 2, and 3 weight percent. A toughening agent at (1, 3, 6,

9) wt.% was incorporated to improve durability and resistance under load, contributing to improved interfacial bonding between polymer matrix molecules without negatively affecting structural homogeneity or thermal properties.

2. Experimental

2.1. Materials Used:

Epoxy Sikadur 52(lp) was bought from the Sika Yapı Kimyasalları A.Ş. company in Tuzla, Istanbul, Turkey. nanoparticles of Zinc oxide, measuring 60 nanometer and with a purity rating of 99 percent, were procured from Shanghai Civi Chemical Technology Co., Ltd. in China. Magnesium oxide nanoparticles (MgO), 60 nm, purity of 99%, were bought from Shanghai Civi Chemical Technology Co., Ltd. in China. Polyethylene glycol-block-polypropylene glycol-block-polyethylene glycol structure (TBCP) was bought from the USA (United States of America). It had a number average molecular weight (Mn) of 2000 g/mol and a functionality of 2.0. Ethanol alcohol, with a purity level of 99.9 percent, was procured from a local marketplace in Hilla, located in Iraq.

2.2. Preparation Samples:

2.2.1. Processing of Raw Epoxy Samples:

Mix the epoxy in conjunction with the hardening agent in a 2:1 mass ratio using a stirring device for a duration of ten minutes. Subsequently, subject the mixture to a degassing system for a duration of 15 to 20 minutes at ambient temperature. Subsequently, transfer the mixture into the prepared silicon mold and allow it to cure at the ambient temperature for a duration of seven days. Figure 1 delineates the procedures for the preparation based on pure epoxy samples.

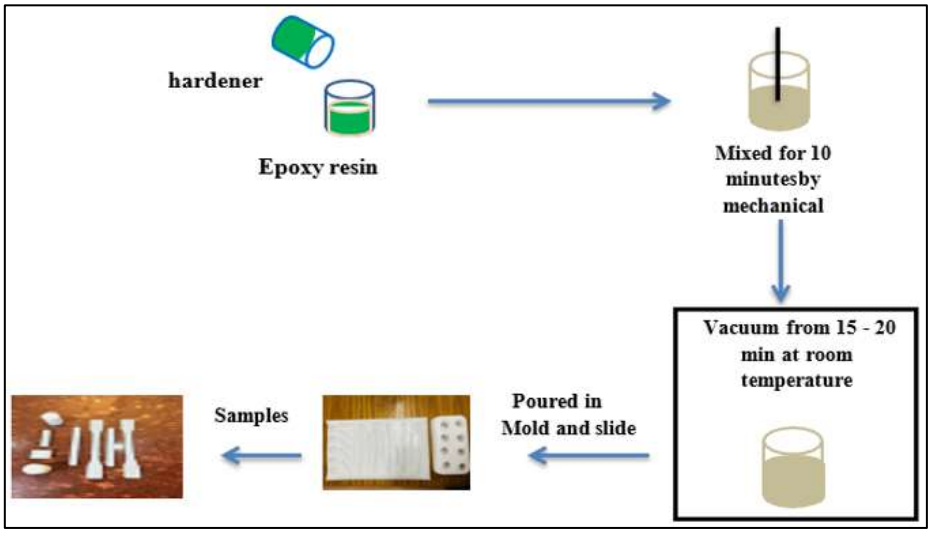

Fig 1. Procedure for processing pristine epoxy resin samples.

2.2.2. Preparation of epoxy blend:

Add various weight ratios of toughening agent (1%, 3%, 6%, and 9%) to the epoxy resin to create modified epoxy systems with toughening agent (TBCP). Use a mechanical stirrer to mix the toughening ingredient into the epoxy for 10 minutes. Then add the hardener at a 2:1 ratio and stir for 10 minutes at 550 rpm using the same mechanical stirrer. Let the resulting

mixture stand at room temperature in a degassing apparatus under vacuum for 15-20 minutes to eliminate any remaining bubbles. After degassing, pour the slurry into silicone molds and allow it to cure at room temperature for seven days. This technique produced various modified epoxy polymer mix samples, as shown in Figure 2.

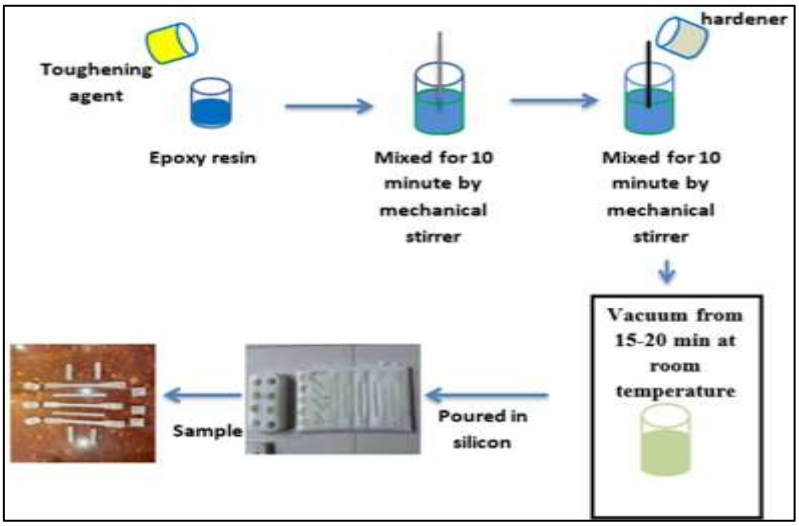

Fig 2. Epoxy's procedure for preparation/ TBCP.

2.2.3. Preparation of Nanocomposites

- Epoxy resin material/TBCP/ ZnO compound (EP/TBCP/ZnO).
- Epoxy resin material/TBCP/ MgO compound (EP/TBCP/MgO).

Initially, material composites were synthesized with varying concentrations (0.5, 1, 1.5, 2, and 3) percent weight of magnesium oxide and nanoparticles made of ZnO (NPs) as detailed in Table 1, below. Dispersed nanoparticles in ethanol using an ultrasonic device at 35°C and energy 40% (sonic frequency 40 kHz) for 45 min, added to the epoxy, and blended with 6% TBCP. Then, the mixture was mechanically mixed for one hour, with heating in an oven at 70° C to volatilize the liquid solvent and ensure good mixing. After that, the blend was weighed before using the degassing system under vacuum for 10 min at 70 °C to cause the solvent to evaporate, and then the mixture was reweighted to ensure that the evaporating solvent had evaporated after using the degassing system under vacuum. The hardener, at a 2:1 ratio, was included and agitated for five minutes utilizing a mechanically driven stirrer. The mixture that emerged was placed in the degassing system under vacuum conditions at the surrounding temperature for thirty minutes in order to remove air bubbles, The liquid was there after put into the silicone mold and allowed to cure at the ambient temperature for seven days. Figure 3 describes the procedures used to prepare the sample.

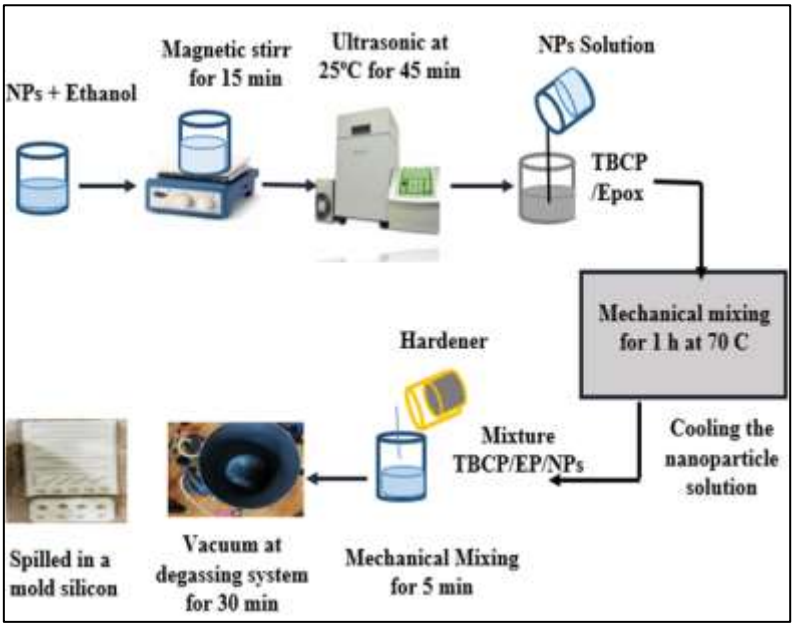

Fig 3. Preparation mechanism of epoxy/ TBCP/ZnO, MgO Nanocomposite.

Table 1. The elements found in specimens.

Sample No.	Sample Code	Sample Composition
1	EP	Pure Epoxy
2	EP/TBCP 1	Epoxy/TBCP 1%
3	EP/TBCP 3	Epoxy/TBCP 3%
4	EP/TBCP 6	Epoxy/TBCP 6%
5	EP/TBCP 9	Epoxy/TBCP 9%
6	EP/TBCP6/MgO 0.5	Epoxy/6%TBCP /0.5% Magnesium oxide
7	EP/TBCP6/MgO 1	Epoxy/6%TBCP /1% Magnesium oxide
8	EP/TBCP6/MgO 1.5	Epoxy/6% TBCP /1.5% Magnesium oxide
9	EP/TBCP6/MgO 2	Epoxy/6% TBCP /2% Magnesium oxide
10	EP/TBCP6/MgO 3	Epoxy/6% TBCP /3% Magnesium oxide
11	EP/TBCP6/ZnO 0.5	Epoxy/6% TBCP /0.5 % Zinc Oxide
12	EP/TBCP6/ZnO 1	Epoxy/6% TBCP/1 % Zinc Oxide
13	EP/TBCP6/ZnO 1.5	Epoxy/6% TBCP /1.5 % Zinc Oxide
14	EP/TBCP6/ZnO 2	Epoxy/6% TBCP /2 % Zinc Oxide
15	EP/TBCP6/ZnO 3	Epoxy/6 %TBCP /3 % Zinc Oxide

2.3. Tests:

2.3.1. Field-Emission Scanning-Electron-Microscopic (FE-SEM) Test:

An analyzing field-emitting scanning-electron-microscopy device, type (Inspect F50 FE-SEM), manufactured by the Dutch manufacturer (FEI). The test utilized tension specimens, focusing on the examination of the sample's fracture region.

2.3.2. Tensile Test:

See Figure 4 for a visual of the tensile specimens that were made in accordance with ISO 527-2 [16]. Employing a 5 Kilo Newton load cell at a velocity of 5 millimeters per minute, the specimens were evaluated at room temperature using the WDW-5E equipment. To get the stress-strain curve, the specimen was subjected to a load until it broke. The following equation was used to compute the modulus of tensile force and strength of tension [17].

$$\sigma = \frac{F}{A} \qquad (1)$$

$$E = \frac{\Delta\sigma}{\Delta\varepsilon} \qquad (2)$$

Where:

σ = strength of tension, MPa.

E = Modulus of Elasticity, GPa.

F = Load, N.

A = Cross-sectional area of the sample, mm^2.

Δσ = σ2- σ1 Stress of sample, MPa.

Δε = ε2-ε1 Strain of sample

Fig 4. Samples for tensile testing.

2.3.3. Fracture Toughness Test:

A fracture strength examination with a one-edge notch beam was performed on V-formed bars to evaluate the durability of the nano-composite material. The specimens in figure (5) were examined using a WDW/5E instrument. The specimens were subjected to a preliminary cutting at the end of the V-section shape, where a "sharp kerf" was established utilizing a hand-held power weight. The entire long has been determined at 45 millimeters at ambient temperature, with a forward speed of 5 millimeters per minute in compliance with ASTM D 5045 requirements. The calculation of stress intensity Kıc was performed by employing the formulas provided below [18].

$$K_{IC} = \left(\frac{P}{BW^{1/2}}\right) f\left(\frac{a}{w}\right) \qquad (3)$$

$$f(x) = 6x^{1/2}\frac{[1.99-x(1-x)(2.15-3.93x+2.7x^2)]}{(1+2x)(1-x)^{3/2}} \quad (4)$$

Where:

K_{IC} = Toughness of fractures (a critical intensity of stress factor), MPa $m^{1/2}$.

P = maximum load, N.

B = thickness of the sample, m.

W = width of the sample, m.

a = crack length, mm.

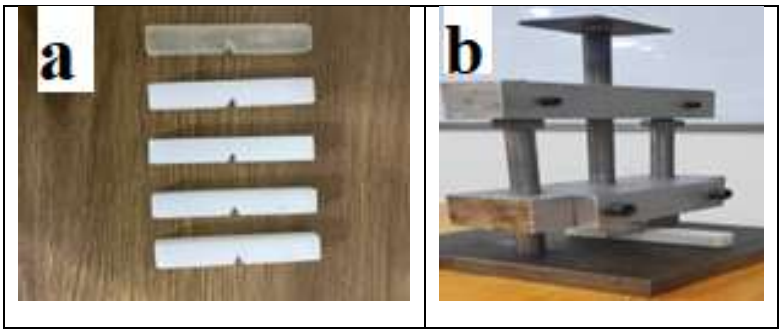

Fig 5. Images (a): The Samples of (SENB) and (b): The approach to generating a crack within the toughness of fracture SENB.

2.3.4. Hardness Shore D Test:

The test for hardness is a crucial method used to evaluate and measure a material's resistance to surface deformation or cavitation. In coating applications, high hardness is essential for preserving surface appearance, as it directly contributes to the coating's resistance and long-term durability. In this study, hardness measurements were performed using a Shore D hardness tester (Model TIME 5431, TH210FJ, China) according to ASTM D2240. The testing procedure involved placing the indenter needle perpendicularly on the sample surface. Each specimen was tested six times at different locations, and the average of these readings was recorded as the final hardness value**.**

2.3.5. Thermal Conductivity Test:

The value of thermal conductibility examination was conducted to assess the thermal conductibility of pure epoxy resin material as well as epoxy strengthened with TBCP, magnesium oxide, and zinc oxide nanoparticles. The parts were assembled with a height of thirty millimeters and a circumference of twenty-five millimeters. There were two holes made, spaced 6 millimeters apart, with every one having a diameter of 1.3 millimeters, for the purpose of conducting a thermal conductivity test. The KD2-Pro, manufactured in the United States of America, was utilized for measuring the degree of thermal conductivity.

3. Results and Discussion

3.1. Field-Emission Scanning-Electron-Microscopic (FE-SEM):

The Figures (6,7) illustrate electron microscope observations of pure material of the epoxy resin, epoxy/TBCP, and epoxy/TBCP nano-composites, respectively at scale 50μm for

all sample. Figure 6a,b small, uniformly distributed dark spherical domains were observed. As the TBCP concentration increased to 6 wt%, these domains became larger, more distinct, and more widely dispersed throughout the epoxy matrix. SEM analysis confirmed that the incorporation of EO–PPO–EO triblock copolymer induced heterogeneity in the system. After increasing the polyol (EO–PPO–EO) content in the epoxy system, the fracture surface was observed to change from a smooth to a rougher morphology. This behavior is attributed to the enhancement of fracture toughness resulting from the formation of fine rubbery domains within the matrix, which absorb fracture energy through mechanisms such as cavitation and localized shear yielding, leading to higher energy dissipation and a more ductile fracture pattern [14].

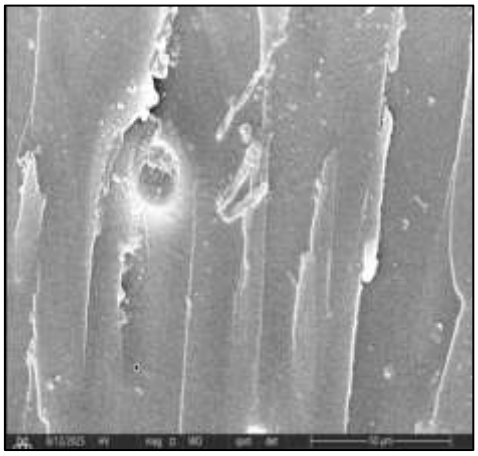

Fig 6. FESEM image of pure epoxy.

The test results showing Figure 7c,d,e,g that adding 0.5% of nanoparticles (ZnO, MgO) results in a rough and regular surface. The observed roughness suggests an effective distribution throughout the epoxy matrix, thereby improving both the mechanical characteristics and the splitting strength of the epoxy. At elevated concentrations of 3%, the formation of clumps and an enhancement in irregular roughness are observed, suggesting inadequate dispersion and reduced structural cohesion, which aligns with a deterioration in mechanical properties [15-19].

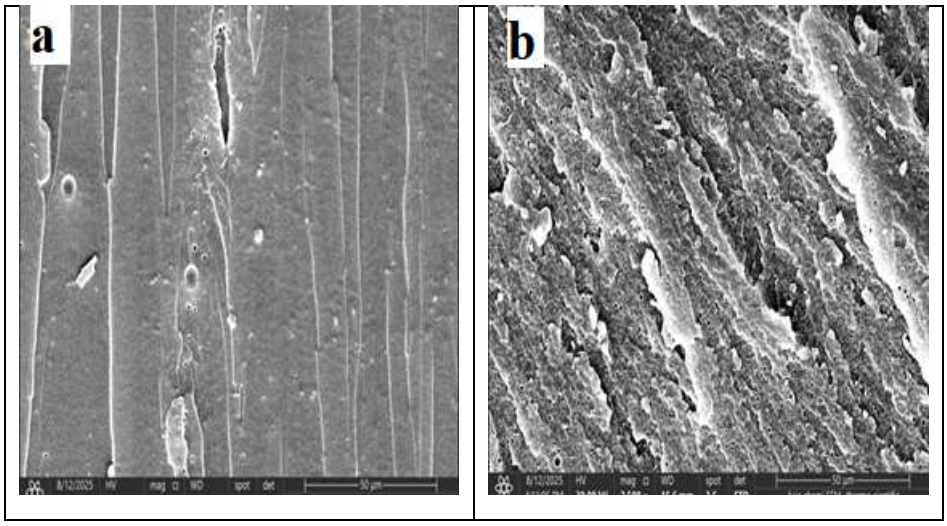

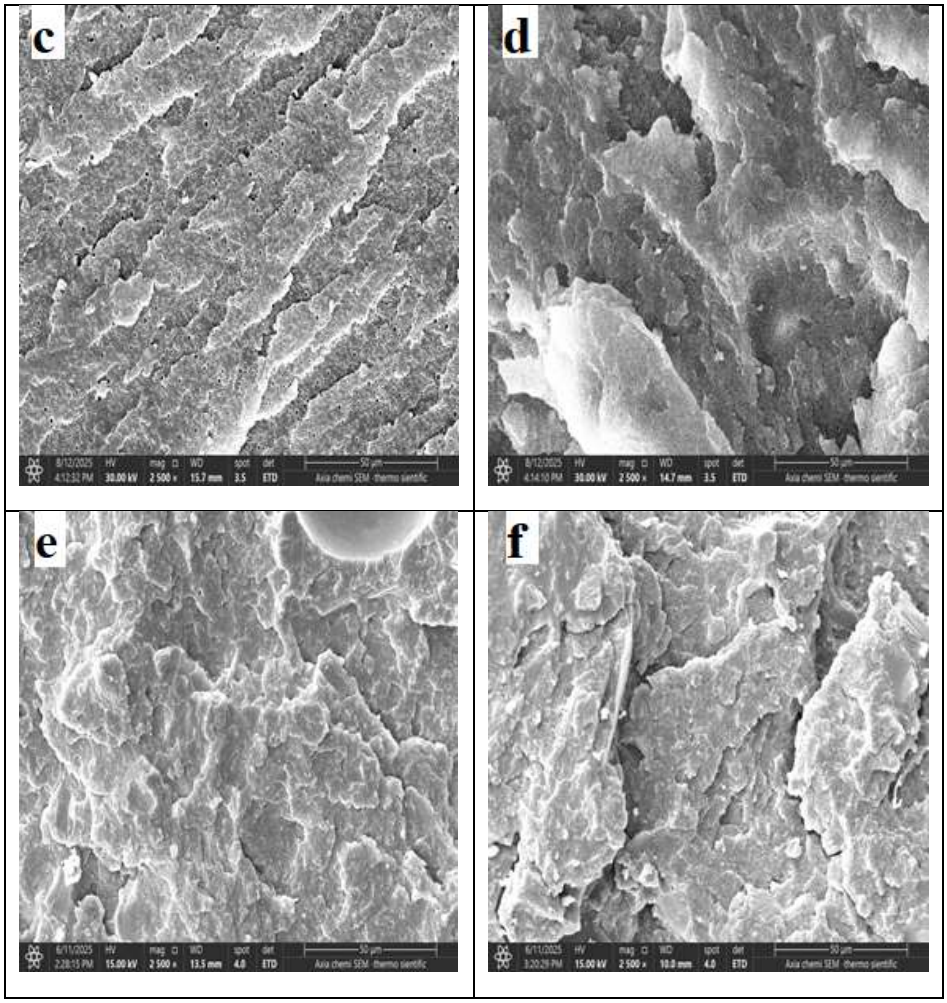

Fig 7. (FE-SEM) pictures (a): epoxy /TBCP with 1 weight percent, (b): epoxy /TBCP with 6 weight percent, (c): epoxy /6% TBCP/ZnO with 0.5 weight percent, (d): epoxy/6% TBCP/ZnO with 3 weight percent, (e): epoxy/6% TBCP/MgO with 0.5 weight percent, (f): epoxy /6%TBCP/MgO with 3 weight percent.

3.2. Tensile Test Results:

3.2.1. Epoxy Blend:

In Figure 8a,b, the results indicate that increasing the TBCP content in epoxy (EP) blends leads to a slight increase in elastic modulus and tensile strength. The improvement in tensile strength and elastic modulus at moderate toughening agent loadings (up to 6 wt%) cannot be attributed to the plasticizing effect. Instead, it results from enhanced interfacial adhesion between the epoxy matrix and the TBCP molecules, leading to a more homogeneous cross-linked network capable of more efficient stress transfer. In this composition, blends act as a toughening modifier rather than a plasticizer. However, at higher concentrations (above 6 wt%), the excessive presence of TBCP induces plasticization, which reduces stiffness and tensile strength due to weaker interfacial bonding and the formation of soft TBCP-rich domains. This improvement is primarily linked to the phase-separated morphology, where TBCP forms uniformly distributed domains within the epoxy matrix. Furthermore, the improved mechanical behavior can be ascribed to the softening effect of the flexible TBCP

chains within the rigid epoxy network, as well as the strong compatibility and interfacial adhesion between the matrix and the dispersed phase [20,21].

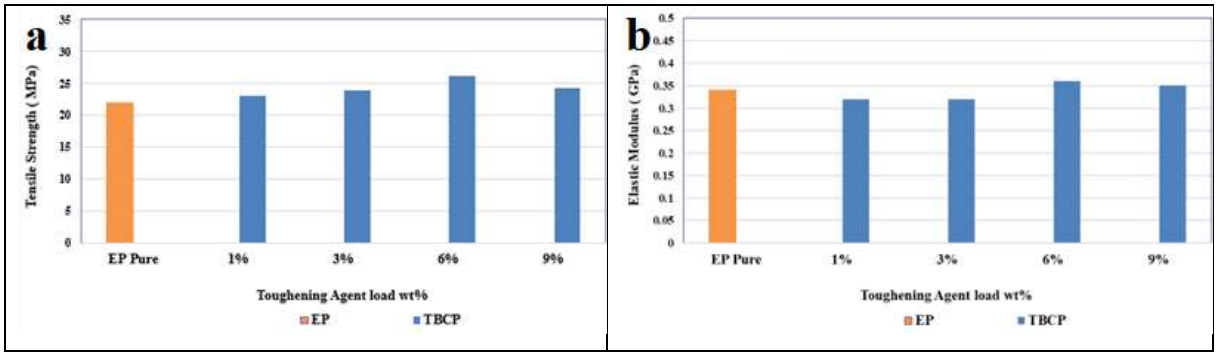

Fig 8. Effect of toughening agent content wt.%, (TBCP) on the(a) tensile strength, (b) elastic modulus of pure epoxy.

3.2 .2. Nanocomposites:

Figure 9 illustrates the correlation between the strength of tensile and the varying percentages of additives (0.5, 1, 1.5, 2, and 3) wt.% for both zinc oxide and magnesium oxide in the epoxy with 6% TBCP blend. The findings indicate that the strength of tensile of zinc oxide/epoxy/6% TBCP nano-composites rises with higher zinc oxide content in comparison to pure epoxy resin. This results from the effective distribution of zinc oxide within the matrix of epoxy and the enhanced mechanical connection with the chains of polymer, which consequently limits their mobility. This limitation enhances the material's ability to withstand stretching when subjected to load, thereby improving its tensile strength. The findings align closely with those presented by T. Raja and colleagues [22]. The addition of MgO to the composite results in a slight increase in tensile strength. This happens because the nano-particles group together in the epoxy material (the matrix) and aren't evenly spread out, which makes the connection between the additive and the epoxy resin matrix weak. The findings align closely with those reported by Qasim Saeed et al. [23]. Overall, 3% of ZnO and MgO nanocomposites demonstrate superior strength of the tensile compared to pure material of epoxy resin and a 6 percent TBCP/epoxy blend, attributed to the robust bonding between magnesium oxide, zinc oxide, and the epoxy matrix.

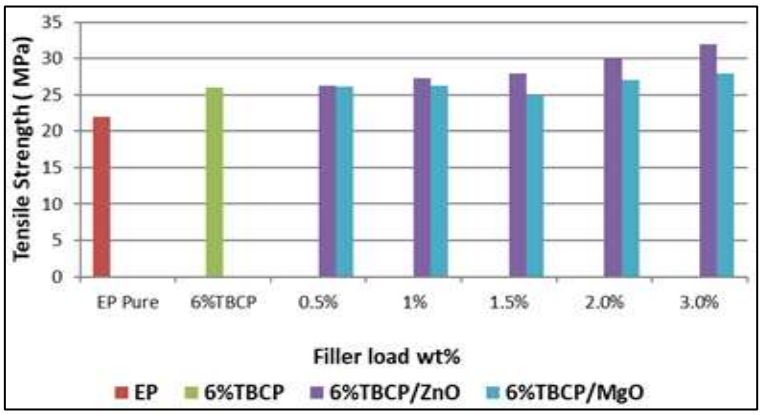

Fig 9. Impact of filler content (weight percent) of ZnO and MgO on the strength of tensile of an epoxy matrix with 6 percent TBCP.

Figure 10 illustrates the correlation between the modulus of elasticity and the ratios of the additives (0.5, 1, 1.5, 2, 3) wt.% of zinc oxide and magnesium oxide in epoxy/6 percent TBCP. Measurements indicate that the modulus of elastic evolves via higher zinc oxide levels in comparison to pure material of epoxy resin and the blends. The inclusion of 3 percent ZnO results in the most significant enhancement in the modulus of elasticity, with values increasing from (0.23, 0.38) GPa for epoxy and epoxy/6 percent TBCP to (0.39, 0.4) GPa for the 3 percent (magnesium oxide, zinc oxide) composite. The high modulus of elasticity of zinc oxide is attributed to the enhanced surface adhesion strength resulting from the way that zinc oxide and the resin binder interact with each other, which subsequently increases the composite's elastic modulus. Epoxy's elastic modulus/6%TBCP/MgO shows no significant improvement, attributed to the limited interaction between MgO and the epoxy/6 percent TBCP matrix, as well as the insufficient ability of the particles to improve their mechanical association. Epoxy's elastic modulus/6 percent TBCP nano-composite exhibits enhancement at elevated concentrations, specifically 3 percent, which is attributed to the effective distribution of clay within the epoxy matrix. The findings align with those reported by Anwar Qasim Saeed et al. [14,15].

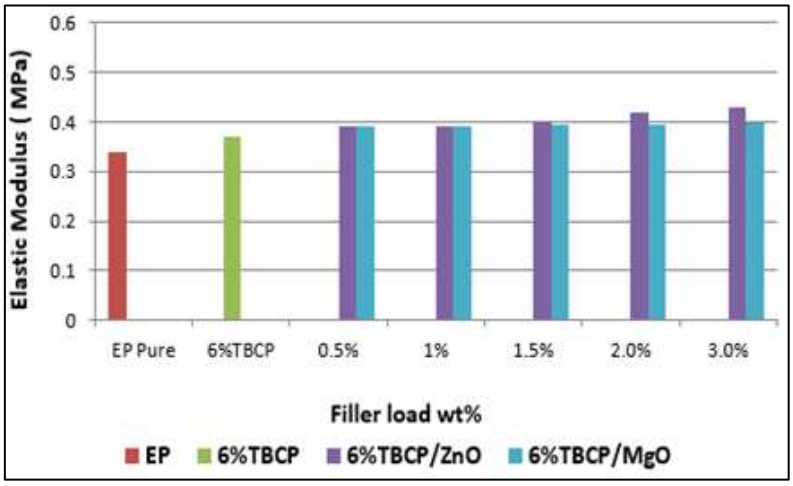

Fig 10. Impact of filler percentage (weight percent) of zinc oxide and magnesium oxide on the modulus of elasticity of the epoxy/6 %TBCP matrix.

3.3. Fracture Toughness (SENB) Results:

3.3.1. Epoxy Blend:

Figure 11 illustrates the fracture toughness (SENB) values of the epoxy/6%TBCP blends. The data reveal that the KIC (critical stress intensity factor) of epoxy resins incorporating polyol is higher than that of neat epoxy. The most notable enhancement occurs at 6 wt% TBCP, where the KIC reaches its peak compared to pure epoxy. The TBCP-modified epoxy system exhibits a distinctly coarse and rough surface morphology, consistent with the observations reported in, as seen in Figure 7a,b. Such surface characteristics are beneficial for improving crack resistance and promoting energy dissipation during fracture [24].

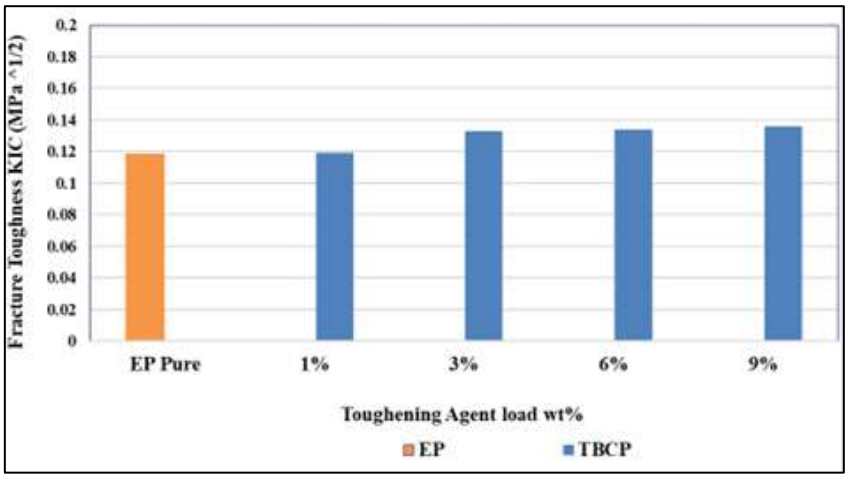

Fig 11. Effect of Toughening Agent wt.% (TBCP) on the fracture toughness of the epoxy matrix.

3.3.2. Nanocomposites:;

Figure 12 illustrates the correlation between the toughness of fracture and the varying addition values (0.5, 1, 1.5, 3) weight percent of zinc oxide and magnesium oxide in the epoxy/6 percent TBCP blend. The findings indicate that the nano-composite loads (epoxy/6% TBCP/ZnO) exhibit a greater K_{IC} compared to pure epoxy, as well as epoxy/6%TBCP and epoxy/6%TBCP/MgO. The fracture toughness increases with the addition of ZnO and MgO nanoparticles in the epoxy/6%TBCP blend. This improvement is mainly attributed to the structural role of nanoparticles, which act as barriers to crack propagation within the polymer matrix, leading to a more efficient distribution of fracture energy and enhanced resistance to crack growth. The epoxy/6%TBCP/ZnO system exhibits higher fracture toughness than the MgO-based system due to the smaller ionic radius and better dispersion of ZnO nanoparticles, which promote strong interfacial bonding with the epoxy chains. The optimum concentration (3 wt.%) provides uniform nanoparticle distribution without agglomeration, resulting in efficient stress transfer and a significant improvement in fracture toughness (Y. N. Baghdadi et al) [25].

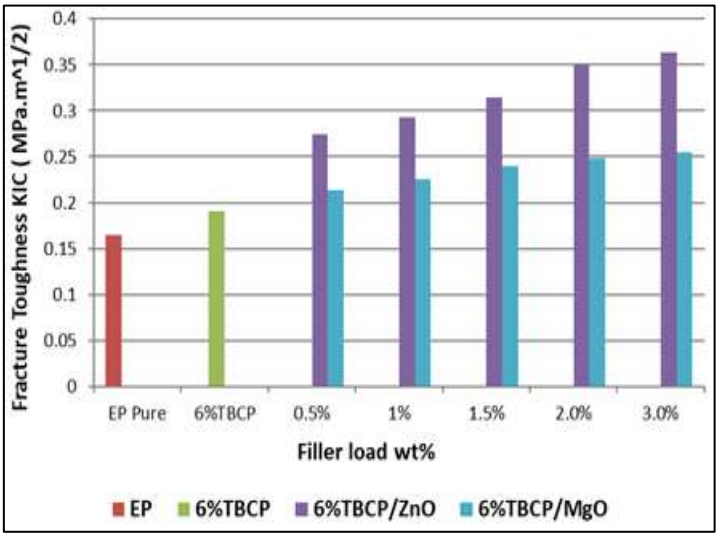

Fig 12. Impact of filler material percentage by weight (zinc oxide, magnesium oxide) on the toughness of the fracture of the epoxy/6 percent TBCP matrix.

3.4. Hardness (Shore D) Test Results:

3.4.1. Epoxy Blend:

Figure 13 illustrates that the incorporation of TBCP into the epoxy matrix at weight fractions up to 6% does not significantly alter the hardness of the composite. This indicates that TBCP acts primarily as a plasticizing agent, improving energy absorption and stress distribution without noticeably affecting the material's surface resistance to indentation. The nano-indentation results show comparable hardness values for pure epoxy and epoxy/6%TBCP systems, suggesting that the influence of toughening agent is more evident in enhancing fracture resistance and overall mechanical toughness rather than in modifying hardness characteristics [26].

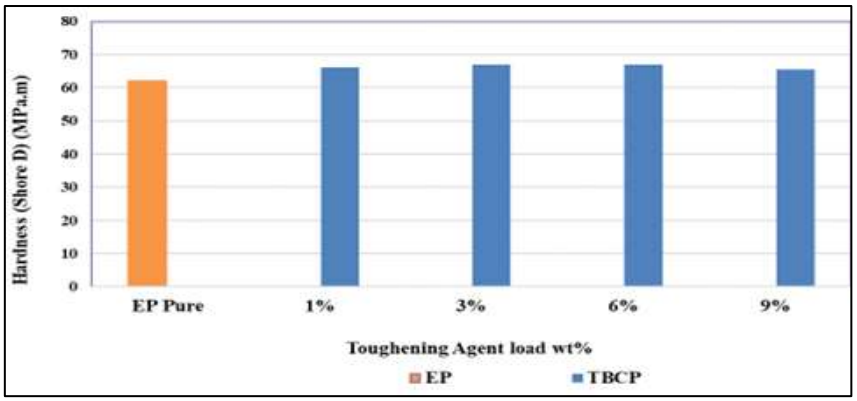

Fig 13. Impact of filler material percentage by weight (zinc oxide, magnesium oxide) on the hardness of epoxy blend.

3.4.2. Nanocomposites:

Figure 14 illustrates the correlation among the degree of hardness and the varying presence amounts (0.5, 1, 1.5, 2, 3) weight percentage of zinc oxide and magnesium oxide in the epoxy/6 percent TBCP blend. The test results indicate that the added filler exhibits somewhat greater degree of hardness. This is because NP, as a denser and harder phase than epoxy, improves the hardness of this enhancement, in which hardness corresponds to the uniform dispersion of nano ZnO and MgO, better matrix-to-particle interaction with and without toughening agent [27,28].

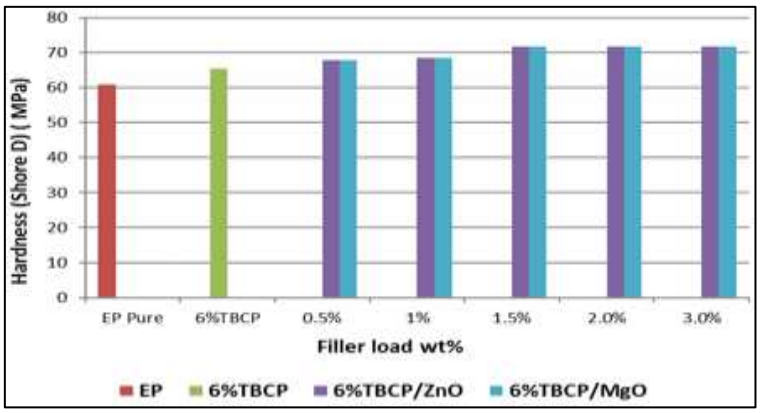

Fig 14. Impact of filler material percentage by different weights of (zinc oxide, magnesium oxide) on the hardness of epoxy matrix.

3.5. Results of Thermal Conductivity Test:

3.5.1. Epoxy Blend:

Figure 15 shows that adding TBCP to the epoxy matrix results in a slight increase in thermal conductivity, as the organic nature of toughening does not provide effective pathways for phonon transport, as ceramic or metallic materials do, making its role in enhancing thermal transport limited and primarily confined to improving mechanical durability.

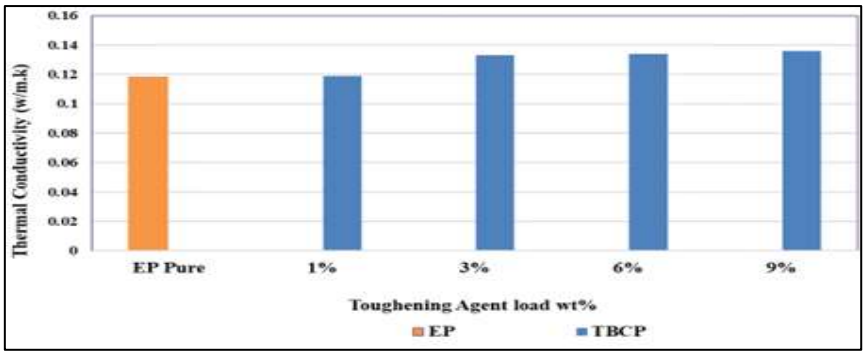

Fig 15. Effect of toughening agent content wt.%, (TBCP) on the thermal conductivity of the epoxy blend.

3.5.2. Nanocomposites:

Figure 16 illustrates the correlation between the conductivity of the thermal and the presence ratios (0.5, 1, 1.5, 2) weight percentage of zinc oxide and magnesium oxide in the epoxy/6 percent TBCP mixture. The findings indicate that the nano-composites (epoxy blend/zinc oxide and epoxy blend/ magnesium oxide) exhibit enhanced thermal conductive properties in comparison to pure epoxy and epoxy with 6 percent TBCP. The conductivity of the thermal of the nanocomposite (epoxy blend/zinc oxide and epoxy blend/ magnesium oxide) shows an enhancement with rising Np content, reaching a peak at 3 percent, with values of 0.267 W/m.k for zinc oxide and 0.316 W/m.k for magnesium oxide. The improvement in the conductivity of thermal of ZnO contributes to an increase in thermal conductivity when incorporated at elevated concentrations. Moreover, the substantial surface dimensions to volume ratio enhances interface interactions, minimizing thermal distribution and boosting the efficiency of phonon thermal transfer. The findings align closely with those reported by Huang et al. [29]. The findings align closely with those presented by Anwar Qasim Saeed and colleagues [30].

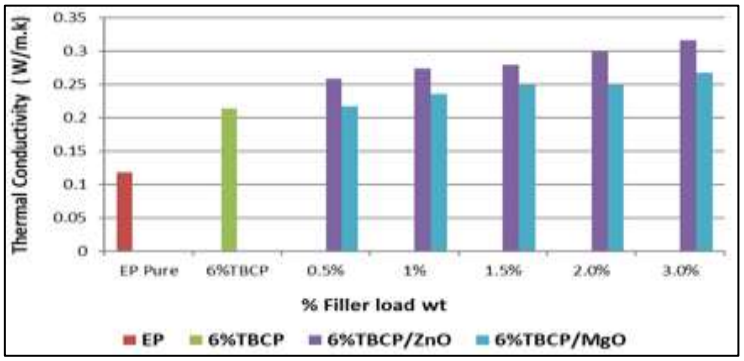

Fig 16. Impact of filler material percentage by different weights of (ZnO, MgO) on the thermal conductivity of the epoxy/6%TBCP.

Table (2): A quantitative comparison between the results of the current study and some previous studies on epoxy resin-based nanocomposites.

Main Improvement Observed	Filler Content (wt.%)	Filler Type	Study
Improvement in tensile strength and mechanical properties as a result of the good dispersion of nanoparticles within the epoxy matrix.	2% wt.	ZnO nanoparticles	Halder et al. [13]
Improvement in tensile strength and some thermal properties of epoxy compounds.	2% wt	ZnO nanofiller	Raja et al.[6]
Improvement in thermal conductivity with a slight increase in hardness.	1-7%wt.	MgO nanoparticles	Saeed et al. [30]
An increase in tensile strength by about 30%, an increase in the modulus of elasticity by about 25%, and an increase in fracture toughness by about 75% compared to pure epoxy.	1-3%wt.	EP/6%TBCP/ZnO EP/6%TBCP/MgO	The current study

4. Conclusions

- The percentage (6% TBCP) gives the best results in improving the fracture toughness epoxy polymer.
- The FE-SEM test shows the roughness of the surface goes up as the amount of filler goes up.
- Composites containing 3 percent oxide of zinc outperformed epoxy/6 percent TBCP, pure epoxy, and nanoparticles of magnesium oxide in terms of fracture toughness, the strength of tensile, and the modulus, according to the results of the testing.
- The degree of nanocomposites' ability to conduct heat considerably exceeds that of epoxy/6 percent TBCP and pure epoxy. The thermal conductivity rises with any rise in nanoparticle concentration relative to pure epoxy.
- A subtle, imperceptible alteration in hardness exists.
- Elevated concentrations of zinc oxide and magnesium oxide yield optimal enhancements in mechanical characteristics and thermal conductive properties.

Acknowledgements

I extend my sincere thanks and appreciation to the Department of Polymer Engineering and Petrochemical Industries, College of Materials Engineering, University of Babylon for their support and effective cooperation, which had a significant impact on the completion of this work, by providing the necessary laboratories and making it possible to conduct practical tests within their available capabilities. I also express my profound gratitude and appreciation to Professor Dr. Zoalfokkar K. Al-obad, my dear supervisor, for his continuous support and valuable scientific guidance, which played a prominent role in completing this study.

Abbreviations

EP	**Epoxy**
FE-SEM	Field emission scanning electron microscopy
KIC	Fracture toughness
TBCP	Tri-block co-polymer
SENB	Single-edge notched bend
MgO	Magnesium oxide
ZnO	Zinc oxide
WC	Tungsten carbide
BN	Boron nitride
EO-PPO-EO	Tri-block copolymer

References:

Negoita, C., Cristache, N., & Bodor, M. (2016). The epoxy resin-History and perspectives. Mater. Plast, 53(3).

Shokry, H. (2014). Molecular dynamics simulation and quantum chemical calculations for the adsorption of some Azo-azomethine derivatives on mild steel. Journal of Molecular Structure, 1060, 80-87.. https://doi.org/10.1016/j.molstruc.2013.12.030

Chen, H., Ginzburg, V. V., Yang, J., Yang, Y., Liu, W., Huang, Y., ... & Chen, B. (2016). Thermal conductivity of polymer-based composites: Fundamentals and applications. Progress in polymer science, 59, 41-85. https://doi.org/10.1016/j.progpolymsci.2016.03.001

Li, X. Y., Zha, J. W., Wang, S. J., Zhong, S. L., Zhang, C., & Dang, Z. M. (2018). Effect of high-thermal conductivity epoxy resin on heat dissipation performance of saturated reactor. IEEE Transactions on Dielectrics and Electrical Insulation, 24(6), 3898-3905. https://doi.org/10.1109/TDEI.2017.006873.

Lee, W., & Kim, J. (2021). Highly thermal conductive and electrical insulating epoxy composites with a three-dimensional filler network by sintering silver nanowires on aluminum nitride surface. Polymers, 13(5), 694. https://doi.org/10.3390/polym13050694

Raja, T., Devarajan, Y., & Kailiappan, N. (2024). Study on enhancing mechanical and thermal properties of carbon fiber reinforced epoxy composite through zinc oxide nanofiller. Discover Applied Sciences, 6(11), 566.

Tomić, M. D., Dunjić, B., Likić, V., Bajat, J., Rogan, J., & Djonlagić, J. (2014). The use of nanoclay in preparation of epoxy anticorrosive coatings. Progress in organic coatings, 77(2), 518-527. https://doi.org/10.1016/j.porgcoat.2013.11.017

Senthil Kumar, M. S., Mohana Sundara Raju, N., Sampath, P. S., & Chithirai Pon Selvan, M. (2018). Influence of nanoclay on mechanical and thermal properties of glass fiber reinforced polymer nanocomposites. Polymer Composites, 39(6), 1861-1868. https://doi.org/10.1002/pc.24139

Nguyen, T. V., Dao, P. H., Duong, K. L., Duong, Q. H., Vu, Q. T., Nguyen, A. H., ... & Le, T. L. (2017). Effect of R-TiO2 and ZnO nanoparticles on the UV-shielding efficiency of water-borne acrylic coating. Progress in Organic Coatings, 110, 114-121. https://doi.org/10.1016/j.porgcoat.2017.02.017

Abdulghani, S. O., Salih, S. I., & Mohammed, A. S. (2024). Toughening of epoxy systems by adding three toughness modifiers as quaternary blends of polymeric materials. Revue des Composites et des Materiaux Avances, 34(5), 621. https://doi.org/10.18280/rcma.340510

Alobad, Z. K., & Akraa, M. A. (2024). EFFECT OF MODIFICATION WITH POLYETHER POLYOL AND LIQUID SILICON RUBBER ON THE MECHANICAL PROPERTIES OF EPOXY

SYSTEM. Kufa Journal of Engineering, 15(3). https://doi.org/10.30572/2018/KJE/150310

Raju, B. N., Ramji, K., & Prasad, V. S. R. K. (2015). Mechanical properties of glass fiber reinforced polyester ZnO nanocomposites. Materials Today: Proceedings, 2(4-5), 2817-2825. https://doi.org/10.1016/j.matpr.2015.07.294

Halder, S., Prasad, T., Khan, N. I., Goyat, M. S., & Chauhan, S. R. (2017). Superior mechanical properties of poly vinyl alcohol-assisted ZnO nanoparticle reinforced epoxy composites. Materials Chemistry and Physics, 192, 198-209. https://doi.org/10.1016/j.matchemphys.2016.12.055

Al Saadi, Z. A. R. A. H., Alobad, Z. K., & Akraa, M. A. (2024). The effect of tungsten carbide nanoparticles on the morphological, mechanical and tribological properties of WC/epoxy and WC/TBCP/epoxy nanocomposite. Journal of Achievements in Materials and Manufacturing Engineering, 124(1), 5-16. https://doi.org/10.5604/01.3001.0054.7215

Peddamallu, N., Nagaraju, G., Sridharan, K., Velmurugan, R., Vasa, N. J., Nakayama, T., & Sarathi, R. (2019). Understanding the electrical, thermal, and mechanical properties of epoxy magnesium oxide nanocomposites. IET Science, Measurement & Technology, 13(5), 632-639. https://doi.org/10.1049/iet-smt.2018.5514

Xiong, J., Wang, S. M., Zhou, W., & Wu, J. G. (2008). Measurement and analysis of ultimate mechanical properties, stress-strain curve fit, and elastic modulus formula of human abdominal aortic aneurysm and nonaneurysmal abdominal aorta. Journal of vascular surgery, 48(1), 189-195. https://doi.org/10.1016/j.jvs.2007.12.053

Ray, K. K., Chegondi, V. J., Roy, U., & Jha, R. N. (2014). Search for rapid quality control of Ni-Cr-Mo low alloy steels using multifaceted approaches for fracture toughness estimation. Advanced Materials Research, 939, 130-137. https://doi.org/10.4028/www.scientific.net/AMR.939.130

Bajpai, A., & Wetzel, B. (2019). Tensile testing of epoxy-based thermoset system prepared by different methods. https://doi.org/10.20944/preprints201907.0143.v1

Şomoghi, R., Semenescu, A., Pasăre, V., Chivu, O. R., Niţoi, D. F., Marcu, D. F., & Florea, B. (2024). The impact of ZnO nanofillers on the mechanical and anti-corrosion performances of epoxy composites. Polymers, 16(14), 2054. https://doi.org/10.3390/polym16142054

Parameswaranpillai, J., Sidhardhan, S. K., Harikrishnan, P., Pionteck, J., Siengchin, S., Unni, A. B., ... & Jose, S. (2017). Morphology, thermo-mechanical properties and surface hydrophobicity of nanostructured epoxy thermosets modified with PEO-PPO-PEO triblock copolymer. Polymer Testing, 59, 168-176. https://doi.org/10.1016/j.polymertesting.2017.01.029

Lavoratti, A., Zattera, A. J., & Amico, S. C. (2021). Effect of carbonaceous nanofillers and triblock copolymers on the toughness of epoxy resin. Polymer Bulletin, 78(10), 5467-5480. https://doi.org/10.1007/s00289-020-03375-1

Masghouni, N., & Al-Haik, M. (2015). Quasistatic and dynamic mechanical characterization of a woven carbon fiber–zinc oxide nanowires–epoxy composite. Polymer Composites, 36(12), 2184-2192 https://doi.org/10.1002/pc.23129

Thamir, A. A. (2018). Enhanced Mechanical, Electrical Properties of the Epoxy Polymer by Adding Hexagonal Boron Nitride Nanoparticles. Indian Journal of Natural Sciences, 8(49).

Bashar, M. T., Sundararaj, U., & Mertiny, P. (2014). Morphology and mechanical properties of nanostructured acrylic tri-block-copolymer modified epoxy. Polymer Engineering & Science, 54(5), 1047-1055. https://doi.org/10.1002/pen.23648

Naous, W., Yu, X. Y., Zhang, Q. X., Naito, K., & Kagawa, Y. (2006). Morphology, tensile properties, and fracture toughness of epoxy/Al2O3 nanocomposites. Journal of Polymer Science Part B: Polymer Physics, 44(10), 1466-1473. https://doi.org/10.1002/polb.20800

Jayan, J. S., Saritha, A., Deeraj, B. D. S., & Joseph, K. (2020). Triblock copolymer grafted Graphene oxide as nanofiller for toughening of epoxy resin. Materials Chemistry and Physics, 248, 122930. https://doi.org/10.1016/j.matchemphys.2020.122930

Narmadadevi, N., Velmurugan, V., Prabhakaran, R., & Venkatakrishnan, R. (2021). Effect of Filler Content on the Performance of Epoxy/Haritaki Powder Composite. In Recent Advances in Manufacturing, Automation, Design and Energy Technologies: Proceedings from ICoFT 2020 (pp. 277-283). Singapore: Springer Singapore. https://doi.org/10.1007/978-981-16-4222-7_33

Khan, R., Azhar, M. R., Anis, A., Alam, M. A., Boumaza, M., & Al-Zahrani, S. M. (2016). Facile synthesis of epoxy nanocomposite coatings using inorganic nanoparticles for enhanced thermo-mechanical properties: a comparative study. Journal of Coatings Technology and Research, 13(1), 159-169. https://doi.org/10.1007/s11998-015-9736-6

Huang, L., Lv, X., Tang, Y., Ge, G., Zhang, P., & Li, Y. (2020). Effect of alumina nanowires on the thermal conductivity and electrical performance of epoxy composites. Polymers, 12(9), 2126. https://doi.org/10.3390/polym1209212

Saeed, A. Q., & Al-Obad, Z. K. M. (2023, July). Investigates the effect of MgO, h-BN, and hybrid nano fillers on the thermal, electrical properties and hardness of an epoxy polymer. In 4TH INTERNATIONAL SCIENTIFIC CONFERENCE OF ENGINEERING SCIENCES AND ADVANCES TECHNOLOGIES (Vol. 2830, No. 1, p. 030025). AIP Publishing LLC. https://doi.org/10.1063/5.0157171

المؤتمر الدولي الثالث للعلوم الهندسية

III. International Conference on Engineering Sciences

ISBN 978-625-92439-3-1

Rimar Academy
Publishing House